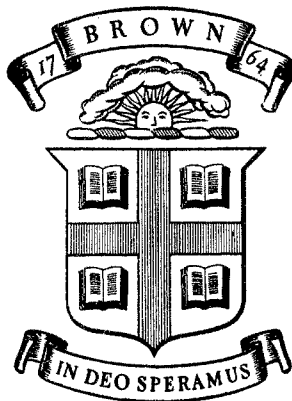


34
ARPA-E-33



Division of Engineering
BROWN UNIVERSITY
PROVIDENCE, R. I.

FIELD ION MICROSCOPY AND A STUDY OF THE
TUNGSTEN-CARBON ALLOY SYSTEM
BY
R. D. FRENCH and M. H. RICHMAN

AD637748

17 AUG 1966
1966
ARPA
ADVANCED RESEARCH PROJECTS AGENCY
DEPARTMENT OF DEFENSE

Department of Defense
Advanced Research Projects Agency
Contract SD-86
Material Research Program

ARPA SD-86
Report E 33

August 1966

DR
ARPA-E-33

I
Field Ion Microscopy and A Study of the
Tungsten-Carbon Alloy System*

by
III
R. D. French[†] and M. H. Richman⁺⁺

Abstract

The Field Ion Microscope has the highest resolution yet attainable; its magnification power being of the order of 10^6 X. A review of technique and theory shows that the microscope has a "built-in" capability of searching a specimen along a third dimension by removal of surface atom layers. Using the FIM to study the tungsten-carbon alloy system, this technique of evaporation allows one to investigate the distribution of carbon about slip bands and the distortion of the tungsten host lattice due to the presence of the carbon interstitial. A model is presented for determining carbon content in carburized specimens. The presence of carbides is discussed along with the effect of the interstitial atom on the tungsten surface layer. Suggestions for improvement and extended work are presented.

*This work is part of a thesis to be submitted in partial fulfillment of the requirements for the Doctor of Philosophy degree in engineering at Brown University. The research was supported by the Advanced Research Projects Agency under contract number ARPA SD86.

+ R. D. French is a research assistant in the Division of Engineering at Brown University, Providence, Rhode Island.

++ M. H. Richman is Assistant Professor of Engineering at Brown University, Providence, Rhode Island.

20060223249

THOMAS J. LIBRARY
ELMT 813
ABERDEEN PROVING GROUND, MD.
STEAP-TL

Table of Contents

Abstract	
1. Introduction	page 1
2. Experimentation	2
2.1. Imaging	2
2.2. The FIM and related equipment	4
2.2.1. Vacuum system	4
2.2.2. Specimen chamber	6
2.2.3. Image recording	9
2.2.4. Specimen preparation	10
2.3. Field ionization	11
2.3.1. Field effect on the potential well	11
2.3.2. Resolution	13
2.3.3. Site enhancement	15
2.4. Field evaporation	17
3. Results	22
3.1. Tungsten-Carbon system	22
3.2. Tungsten-8At.% Carbon	25
3.3. Tungsten-16At.% Carbon	27
3.4. Tungsten-48At.% Carbon	27
4. Discussion	28
5. Summary	30
References	32
Appendix	1A
List of Figures	5A

1. Introduction:

The Field Ion Microscope, created in 1951 by E. W. Muller⁽¹⁾ as an outgrowth of his earlier Field Emission Microscope⁽²⁾, offers a resolution on the order of atomic spacing. The metallurgist now has a chance to observe the effects of various macroscopic and microscopic treatments of a specimen with the highest magnification possible. While it is true that FIM design and operation embody several disadvantages, the greatest advantage is its capability for direct observation of events occurring on an atomically clean surface. Such events would otherwise be followed by beam scattering techniques. It is the intent of this report to present the FIM as a research metallurgist's tool, explore its disadvantages in this respect, and to report on a study of the effects of the carbon interstitial in tungsten, a project currently underway.

The tungsten-carbon binary system provides a possibility for studying diffusion of an interstitial in a bcc structure at high temperatures. The Field Ion Microscope provides a chance to observe the structural effects of adding a few carbon atoms to the tungsten host lattice; and, at higher carbon concentrations, the expected precipitation of one or more of the carbides having a known structure. Prestraining specimens before etching the shape required by the microscope introduces a number of defects which are often identifiable and can be traced in depth by the process of field evaporation. It has been the object of this preliminary work to develop a means of introducing carbon in such a way that the results can be analyzed in terms of structural changes from an easily identified reference frame, a clean tungsten ion image. Further goals include locating and identifying carbides by structure and the effects of deforming the various

alloys. A model for a rough determination of carbon content is presented, and the results of several alloy experiments based on this model are discussed.

2. Experimentation:

2.1. Imaging:

Let us first discuss the method by which an image is formed. A more detailed coverage of the ionization process will follow in a later section. A cutaway drawing of the microscope tube in Fig. 1. shows the positioning of the specimen and the means by which the phosphor screen is grounded. When a high positive potential is placed on the needle-shaped specimen, a field is created at the tip which, if the radius of the tip is of the order of 10^2 \AA to 10^3 \AA , is enhanced locally 4 \AA to 5 \AA above each atomic protuberance. If a gas is present, each gas atom sensing the presence of the electric field is attracted to the tip in dipole form and eventually suffers collision at the surface, giving up a portion of its energy (see Fig. 3.). This energy E , is given as a sum of its thermal energy and the energy due to the field:

$$E = kT + \frac{1}{2} \alpha F^2 \quad (1)$$

where k is Boltzmann's constant, T the temperature, α the polarizability, and F the field. If an amount of energy greater than kT is given up, the atom will be trapped by the field and will rebound only a short distance before returning to the surface where it undergoes another collision. This process repeats itself over and over, the atom gradually migrating toward the weaker field at the shank until, by chance occurrence, it passes into one of the shallow (0.1 \AA) regions located a short distance

above each surface atom where the field is high enough to strip off an electron. The velocity of this atom must be low enough for it to spend sufficient time in the ionization zone for ionization to occur. It then becomes charged and is repelled from the tip to the screen following the force lines, which are everywhere perpendicular to equipotential lines. The energy of this fast moving ion is given up to the phosphor which in turn re-radiates the energy at a characteristic wavelength somewhere in the visible spectrum. Since each atomic protuberance on the specimen surface has a capability of creating a similar effect, although not necessarily of the same magnitude, the phosphor screen will then depict a scene from the specimen surface, enlarged as a result of the diverging force lines acting over the specimen to screen distance. This magnification is given roughly as the specimen to screen distance divided by the tip radius and is typically $10 \text{ cm}/10^{-5} \text{ cm} = 10^6 \text{ X}$. This would indicate that with the proper dimensions every atom on the surface would be imaged. That this is not the case is demonstrated by closer packing of the atoms causing interference among the individual high field regions and a resultant image blurring. Some fields show up as dark areas surrounded by bright rings. The rings may or may not be divisible into individual image points, but they simply represent concentric layer edges or steps where field enhancement is strongest. These are often likened to elevation lines on a contour map, and it is through them that a tip radius can be determined knowing interplanar spacing. For example in a cubic lattice, if the angle between plane normals is γ and the spacing between planes for which a number of rings are visible is d , the tip radius r (in Angstroms), is given by;

$$r = \frac{nd}{1 - \cos \gamma} \quad (2)$$

where n is the number of rings counted between poles separated by the angle γ . From a tungsten image (Fig. 4.) where the near central pole is [011] and the spacing between {011} planes is 2.23 \AA , the radius as calculated from the [011] pole to the [112] pole ($\gamma = 30^\circ$) is;

$$r = 16.7 n_{(011-112)} \text{ \AA} \quad (3)$$

and from the [011] pole to the [123] pole ($\gamma = 19^\circ 6'$);

$$r = 40.5 n_{(011-123)} \text{ \AA} \quad (4)$$

Analyzing the entire surface, one finds that the radius varies somewhat. This is an indication of faceting and tip asymmetry, showing that the tip in fact is not a hemisphere and as a result is usually assigned an average radius. Dark areas are regions where the threshold field for imaging has not been reached. It is now left to the remainder of this section to describe the apparatus and working conditions necessary to achieve this phenomenon. Subsequent sections will show how the electric field can be used to advantage in cleaning the surface and revealing a third dimension.

2.2. The FIM and related equipment:

2.2.1. Vacuum system

The microscope used in this work is, like most, of the home-grown variety based on earlier models used by others^(1, 4, 5). A sketch and photograph of the equipment appear in Fig. 2. If it is in the interest of the experiment to maintain a surface free of contaminants over reasonable lengths of working time with no field on the specimen, it is worthwhile to eliminate every joint possible while those that remain should

be of the stainless steel flange type with bakeable metal seals. As will be shown, however, one of the characteristics of the microscope is that the specimen surface remains clean as a result of the applied field. In this study the effects to be observed were applied outside the microscope so that the field, once applied, need not have been removed. The system then has a number of ground glass joints covered lightly with Apiezon N vacuum grease. To avoid possible buildup of this contaminant, thereby preventing fluorescence at high voltages, joints are wiped clean with lint-free paper and swabbed with ether after each opening. The system is pumped to $\sim 10^{-6}$ mm Hg using a 3 inch oil diffusion pump; pressure is monitored with an NRC model 524 cold cathode gauge set in the metal tubing somewhat removed from the microscope chamber. The relatively small tubulation, a succession of right angle corners, and the distance of the chamber from the pump all tend to eliminate backstreaming completely, an absolute necessity. On the other hand, these same factors contribute to long pumping times. Even with a bakeout of the getter tube and phosphor screen, outgassing the getter and filament, and using liquid nitrogen to trap the diffusion pump, six hours are required to reach a residual pressure of 10^{-6} mm Hg. It is therefore important that specimens be carefully prepared, a subject that will be treated in a later section. Final pressure is obtained by heating a titanium wrapped tungsten loop in a tube immersed in liquid nitrogen. This is done with the diffusion pump sealed off from the system as close to the specimen chamber as possible. The system is then ready for the admission of the gas to be ionized, hereafter called the imaging gas. While several gases can be used depending largely on the relation of their ionization potentials to the evaporation potential of the specimen and on the temperature of the specimen, this laboratory has restricted its use to helium which is admitted by passing tank gas around

a heated quartz tube connected directly to the system. Helium passes readily through heated quartz and Vycor, its leak rate depending on the temperature. Hydrogen can also be passed directly into the system in this manner using a nickel or palladium tube.

The working pressure of the microscope is bounded by two facts. At low pressures the rate of ionization at the specimen surface is governed by the supply of atoms to the surface. A reduction in the number of ions decreases image brightness. At high pressures the mean free path of the ion is reduced considerably creating a large amount of scatter and a blurred image on the screen. For helium an acceptable working pressure was found to be between one and three microns⁽¹⁾. It must be kept in mind that the pressure indicator is generally calibrated for air, consequently gage pressure should read 0.15 to 0.5 microns.

2.2.2. Specimen chamber

The methods used in this laboratory for preparing a microscope tube are somewhat different from those previously described by others⁽⁴⁾ and are worthy of mention. Fig. 1. shows such a tube with the cold finger in place. Since it is necessary that at least the lower part of the screen tube be conducting, we have coated the entire inside of the tube (A) with a layer of transparent tin oxide, masking off only the ground joint areas, and using the diffusion pump connection (C) as a convenient spot for a ground connection. Grounding is completed through a tungsten spring clip (I) in contact with the SnO_2 surface in the tube and an inner aluminized surface (K) on the glass connecting arm (C) in the diffusion pumpline. A tungsten lug (M) sealed in uranium glass passes through the wall of this arm to the outside where standard electrical connections (N) complete the path. The SnO_2 coating, once applied, seldom requires removal

since it withstands all ordinary usage and is attacked only by hydrofluoric acid. It is a particularly convenient coating to use where current densities are low. Application consists of heating the tube in a horizontal position to 450°C to 500°C where upon a fine spray mist of SnCl_2 in alcohol is introduced through the neck with an air gun. It is not necessary to enter the bottle to spray the lower chamber if the mist is fine, but the low temperature of the solution requires that the spray be applied in short bursts and that the bottle regain the high temperature after each burst. Two or three such cycles followed by several hours of oven cooling give a fairly uniform coating where the screen area to grounding point resistance is of the order of seven to ten thousand ohms.

A phosphor screen can withstand the heavy ion bombardment for many working hours, but the fact that it does deteriorate suggests that it be easily replaceable. A thoroughly mixed undersaturated solution of Willemite phosphor in alcohol is introduced to the screen area with a pipet, keeping the bottle in an upright position, resting on a smooth, flat, hard, level surface. A little experience will indicate how much should be applied. The bottle is then swirled in small circles without lifting from the surface until the coating is uniform. The alcohol will evaporate in a matter of hours at room temperature leaving an adherent screen. This screen is readily removed by wiping but due to its inaccessability it is easiest to introduce clean alcohol and several glass beads of a few millimeters diameter which can be swirled about and poured off. The procedure, while time consuming, is simple enough to neglect concern for error.

The cold finger, as shown in Fig. 1., is intended for use only with nitrogen in liquid (77°K) or solid (63°K) form. Liquid nitrogen can be solidified by lowering the pressure to ~100 mm Hg. As will be shown in a later section, lowering the specimen temperature in this manner improves image resolution. For still lower temperatures a double dewar system must

be used⁽¹⁾. Etched needle-shaped specimens are spotwelded to 6 mil tungsten wire hairpins and plugged into tungsten coils sealed in the bottom of the finger. Tip temperature during heating cycles may be measured optically through the screen tube wall but with considerable inaccuracy. More precise work requires an additional pair of tungsten leads to be spotwelded to the hairpin for resistance measurements⁽⁴⁾. The lower end of the finger has a ground joint for intimate contact with an aluminum cone-shaped sleeve truncated just below the end of a specimen in a normal configuration. Vertical positioning of the specimen is not precise although concentricity should be maintained to keep the image on the screen. The purpose of the sleeve is largely to cool the impinging gas.

A 0 to 30KV potential is provided by an NJE power supply continuously variable with a minimum increment readout of 200V as purchased. This has been modified with a variable series step of 2500V having a minimum increment readout of 25V. Beam currents are in the 10^{-9} ampere range and as such, hazardous x-rays are not produced under normal conditions⁽¹⁾. Tip size is limited by the range of the power supply to about 1400 \AA radius. This is determined from an equation for the average field over the specimen;

$$F = \frac{V}{kr} \quad (5)$$

where k is a slowly varying parameter, dependent on the radius, and except for very small tips is taken as 5. For a freely suspended sphere, $k = 1$ but consideration must be given to the change in field distribution in the presence of the shank. Gomer⁽⁴⁾ provides a description of this parameter with further references.

2.2.3. Image recording

Recording the image is no small problem although considerable progress has been made^(6, 7). A number of camera, lens, film combinations have been reported^(1, 4, 5) and our own use will add to the growing list of possibilities. Ion excited images are quite dim, requiring open lens photography and a film particularly sensitive to the narrow region of phosphor response, the latter perhaps more important than the use of a "fast" film having an inherent noticeable graininess. The phosphor used in these experiments was Willemite, having a peaked response at about 5200 Å. Kodak Recording Film #2492 and Kodak Spectroscopic Film #103a-G reduced exposure time by a factor of 1.5 to 2 from that of Tri-x film although the latter is reasonably fast with an ASA rating of 400⁽⁸⁾. The #2492 film had the shortest exposure time but noticeably more grain than the #103a-G. All films were developed in fine grain developers such as Diafine, Kodak D-76, or Ethol; the final combination being #103a-G film developed in Ethol. The camera is a Nikon F mounted with an F 1.4 lens and suitable extension rings for closeup work. Focusing is a two-fold problem. Microscope focusing is performed by adjusting the applied voltage. An overvoltage blurs the image by causing ionization to take place over a more continuous surface farther away from the tip. Lowering the voltage decreases image brightness. The actual voltage for image recording purposes is somewhat lower than that required to produce the maximum number of artifacts with minimum background and lies in a narrow region of about 1% of the best image voltage⁽¹⁾. Focusing the camera is no less a task although it need only be done once unless the screen is moved. The camera is mounted in an inverted position on its own enlarging stand. By placing a locking ring below the support arm (see Fig. 2.), the camera is roughly focused and positioned so that it can be swung away and

back without changing the camera to screen distance. By placing a bar of suitable thickness flat against the bottom of the screen chamber and shining a beam of light from one side so that the beam casts a shadow on the Willemite, an image is created in close approximation to the ion image and the lens can be focused on this even in a lighted area. The camera is demountable for film loading and, providing the lens setting is not changed, it can be remounted in focus.

2.2.4. Specimen preparation

Specimen preparation involves a number of steps both in and out of the microscope. In this particular study a first image is obtained from a clean tungsten specimen. Carbon is added and diffused into the tungsten at elevated temperatures and a new image is formed. Initial tungsten specimens are prepared from 6 mil wire spotwelded to a 6 mil tungsten wire hairpin support using 100 mesh titanium powder as an intermediate. Since titanium and tungsten alloy readily, this combination helps to reduce a brittleness inherent to tungsten heated in air. A 5% NaOH electrolytic bath using 10 to 20V dc is used to shape the 6 mil wire into a point. Any etching action occurs more rapidly within the meniscus formed on the wire at the liquid surface as a result of higher oxygen pressure. By continually moving the specimen vertically in and out of the bath, a long slender taper with a sufficiently sharp point will develop. Voltage must be low enough that grain boundaries are not severely attacked or that pitting does not occur, both of which lead to premature specimen failure under the hydrostatic stress imposed by the electric field. This stress, σ , is given by;⁽⁴⁾

$$\sigma = \frac{F^2}{8\pi} \quad (6)$$

in dynes/cm² when F, the field, is expressed in esu. At imaging fields this turns out to be of the order of the elastic constant of the specimen. Normally this stress acts as a hydrostatic tension which would not affect local discontinuities such as twins or sub-boundaries. If, however, a pit or groove exists in the surface, a large shear component develops which leads to failure. It is only the whisker-like dimensions of the tip which enable it to withstand the high stresses.

Following a wash in distilled water and then alcohol, the newly etched tip is inserted in the microscope where a low temperature (1200°C) annealing treatment is applied momentarily, the surface being subsequently cleaned and smoothed by the techniques of field evaporation to be described later. As soon as a complete image can be recorded, the specimen is removed to a vacuum evaporating chamber where carbon is deposited in one of two ways. A mounted specimen may be fastened to a turntable in the presence of evaporating carbon. This insures full coverage, eliminating possible preferential diffusion of carbon over the tungsten surface later, but the procedure is done cold. Diffusion at ~1500°C is performed in the FIM. In another method, a stationary specimen is heated to ~1500°C during deposition of carbon, and the direction of deposition is noted. Both procedures are performed in the 10⁻⁵ mm - 10⁻⁶ mm Hg region, and will be differentiated hereafter by terming the cold process "carbonizing" and the direct diffusion process "carburizing".

2.3. Field Ionization:

2.3.1. Field effect on the potential well

The process by which an image gas atom becomes charged is called field ionization, and it can only occur within a shallow region at a critical distance from the metal surface as previously indicated. Referring to Fig. 5

which shows a simple case of a hydrogen atom having only one electron, we see that at a distance from the metal surface large compared with atomic dimensions, the electron in the gas atom lies deep in its own potential well, not feeling any effect of the applied field. As this atom approaches the metal surface, a distortion of the well takes place due to the applied field; enhanced toward the image gas atom nucleus and diminished toward the metal surface so that a lower energy barrier results. At some critical distance from the surface this barrier becomes thinned sufficiently so that the electron can tunnel through to the metal if an available state exists; that is, if the electron assumes an energy position higher than the existing Fermi level, μ . Closer to the metal surface than this minimum distance the barrier has thinned even more, but the ionization potential, I , has increased so that the electron in the gas atom is below μ and no available states exist for tunneling to occur. Since ϕ , the work function of the metal, gives the position of μ relative to a datum level from which I can also be defined, this critical distance for tunneling can be approximated by balancing the effect of the applied field on the depth of the potential well with the difference between I and ϕ ;

$$FX_c = |I| - |\phi| - 3.6 \times 10^{-8} q^2/X_c \approx |I| - |\phi| \quad (7)$$

where X_c is the critical distance and $3.6 \times 10^{-8} q^2/X_c$ is an image term arising from ion interaction with the surface after tunneling has occurred. This latter term is small and the critical distance is usually given by:

$$X_c = \frac{|I| - |\phi|}{F} \text{ cm} \quad (8)$$

At high fields atoms will not penetrate the ionization region and all

particles will be ionized before reaching the tip. Beam current is then restricted by the supply of gas atoms which is 5 or 6 times greater than the number calculated from gas kinetics because of the formation of dipoles from the atoms in the vicinity of the tip and the resultant interaction⁽⁹⁾. At low fields the supply exceeds the ionization rate and beam current will be determined by an equilibrium number of gas atoms near the tip which in turn is given by a Boltzmann factor arising from the polarization energy of atoms in the high field region⁽⁴⁾. At intermediate fields the situation is that previously described in this report where an impinging atom collides with the surface, rebounding with less velocity if it has imparted some thermal energy to the tip. At this lower velocity, the atom will now spend more time in the high field region and stands a greater chance of being ionized. If the rebound velocity is high enough it may escape the field entirely; if not, it will repeat the collision process a number of times until it is either ionized or it passes out of the effect of the high field at the shank of the specimen. This depends on the hopping height. If rebound height is less than x_c , there is no chance for ionization.

2.3.2. Resolution

What does this mean to resolution? A heavy ion suffers little diffraction effect due to its short wave length, so image resolution must depend on either the transverse thermal velocity component imparted to the atom on collision with the tip or on the field distribution at x_c . Since the image gas atoms would be expected to obey Boltzmann statistics at microscope operating pressures, they would have a strong temperature dependence. Cooling the tip then regulates the thermal velocity imparted to the atoms

therefore;

$$v_t = \left[\frac{2kT_{tip}}{m} \right]^{\frac{1}{2}} \quad (9)$$

Radial velocity is largely that imposed by the field, and is given in the same manner;

$$\frac{1}{2} mv_r^2 = \frac{1}{2} \alpha F^2 \quad (10)$$

$$v_r = \left[\frac{\alpha}{m} \right]^{\frac{1}{2}} F \quad (11)$$

If a path is plotted from tip to screen for an ion having both of these velocities, the ion will be found to have deviated from a straight line collision point to some other point laterally removed from the first by an amount dictated by the transverse velocity⁽⁵⁾. This is shown in cross section in Fig. 6. where possible displacement paths ultimately describe a figure of revolution in space and an enlarged scattering disk at the screen. The resolution, δ , is given by;

$$\delta = 4r\beta (kT/e)^{\frac{1}{2}} \quad (12)$$

where r = tip radius, k is Boltzmanns constant, T the temperature, V the tip potential, and e the electronic charge. β is an image compression factor resulting from the effectiveness of the specimen shank in causing the lines of force to line up with the longitudinal axis thus squeezing them together and reducing the magnification by $1/\beta$. For $r = 10^{-5}$ cm, $\beta = 1.5$, and $V = 10^4$ v, the resolution is calculated to be 2.4 Å at 20°K or 10 Å at 300°K. Therefore the effect of the transverse thermal velocity can be minimized.

It turns out, however, that actual resolution is limited by the resolution of high field "spheres" at the high field surface. These spheres are given the radius x_c and any two adjacent atoms on the metal surface are

said to be just resolvable if these spheres only slightly overlap.

At tangency the resolution is given by;

$$\delta = 2 X_c \quad (13)$$

so the intersection is described by;

$$\delta = 2\epsilon X_c \quad (14)$$

where ϵ is a constant and lies between 0.5 and 1.0. Ultimate resolution is $\leq 4 \text{ \AA}$ and this is borne out experimentally.

2.3.3. Site enhancement

Fig. 7. is a partial sketch of a tip cross section showing application of this principle in a comparison of closely packed and more loosely packed planes. Equi-potential lines above the close packed planes tend to smooth out as the equi-potential circles about the atoms increase their overlap. From this model, one can see how an atom or atoms out of place can enhance or diminish the field creating irregularities in the screen image.

It is well to consider what might be expected to cause ionization besides the atomic steps created by stacking atom planes in a pyramidal fashion. Certainly one would expect a planar defect emerging within the field of view to create a linear distortion either enhanced or diminished depending on whether the defect was elevated or recessed. In fact, such lines are readily observed in grain boundaries^(10,11,12) and slip bands⁽¹³⁾. Recently Ranganathan et al. published a report on image streaking,⁽¹⁴⁾ an irregularity sometimes caused by stacking faults or grain boundaries. An example of the latter appears in Fig. 8. Two tungsten crystals both having

a near central {011} pole make up the asymmetrical tip sketched in Fig. 9. A slight overlap of the separate images occurs due to the presence of a step at the boundary created by the sudden change in radius. This is more easily seen by the occurrence of a streak in the same location as the threshold of field evaporation is approached⁽²⁴⁾. Streaking in asymmetric tip images has also been considered by Brandon⁽²⁵⁾ and his arguments cast doubt on the assumption that steps can only exist at the intersection of planar defects with the surface.

The plane of this boundary is of the {001} type. On the surface the crystal combination can be described by either a counter-clockwise rotation of $\sim 75^\circ$ about the $[011]_A$ pole and a translation along a $\langle 111 \rangle$ direction or by a simple ccw rotation of $\sim 87^\circ$ about a pole near $[134]_A$. The boundary is quite complex in character having a low number of coincidence sites in the vicinity of the $(010)_B$ planes and a higher number around the (011) planes.

Vacancies and interstitials create point defects in the equi-potential surface. The most frequent and easily understood observations in this category have emerged from studies of radiation damage⁽³⁰⁾. Interstitials are of particular importance to this study, so let us first consider what happens when an atom is dislodged from its place in the lattice. Fig. 10., adapted from Muller⁽¹³⁾, shows that such an atom must present itself on the surface or move into an interstitial site where it causes a bulge in the surface layer. Here, of course, we are not concerned with vacancies left behind nor with any defect buried too deep to affect the surface layer. In the first case, a bright dot would appear on the screen appearing as a single easily resolvable point defect overlying a normal image. The interstitial, however, disrupts a local area smearing the brightness due to the surface bulge. If the interstitial is an atom from the host lattice or an impurity of similar size, this picture holds quite well. In the

case of carbon in tungsten where the carbon atom is roughly half the size of the tungsten atom, a reduced effect would be expected where "surface" and "just under the surface" impurities would be hard to differentiate. This will be shown in a later section.

2.4. Field Evaporation:

Field desorption and evaporation are the terms used to describe the removal by application of a high field of adsorbed surface material or atoms of the host lattice respectively. When the field is high enough, surface atoms may be pulled free and ionized. This process enables the microscopist to achieve atomically clean surfaces, shape the tip having small surface irregularities, and by careful removal of layers of the base metal, achieve a third dimension in looking "into" the specimen. Adsorbed oxygen can be removed from a tungsten specimen by heating the tip above 1500°K, but this may cause excessive blunting of the tip through surface migration of tungsten atoms. A high field can perform the same task; and if the field is not lowered sufficiently, a barrier is interposed between the metal surface and free oxygen atom such that the oxygen will not be re-adsorbed. This, of course, pertains to other contaminants none of which can be accommodated on the metal surface if the field is over 350 megavolts/cm. Since the image field for helium is ~450 Mv/cm, an atomically clean surface is present under normal imaging conditions. Fig. 11 a.-d. is a succession of photographs showing the desorption effect. Loosely attached adsorbants are quickly removed, restoring the clean tungsten image. It cannot be emphasized too strongly that the nature of the evaporating or desorbing material determines surface structure; and that some understanding of desorption theory is necessary for image interpretation.

As suggested by Muller⁽¹⁶⁾ and later by Gomer and Swanson⁽¹⁷⁾, field

evaporation is taken to be a special case of field desorption. The barrier to be overcome in removing a surface atom contains first an intrinsic hump which can be described by a thermionic cycle wherein the surface atom is taken over its vaporization energy barrier, ionized; and the electron removed is returned to the metal surface. This energy barrier, Q_o , is given by;

$$Q_o = \lambda + I_1 - \phi \quad (15)$$

where λ = heat of vaporization, I_1 = first ionization potential, and ϕ is the total work function (negative since the electron is being returned from infinity, hence a gain in energy). Here only the singly charged ion is admitted. With no applied field the atom rests comfortably in its potential well at a minimum separation distance as shown in Fig. 12a. If ionization were to precede evaporation then it would be complete at some distance out from a stable position whereupon the applied field distorts the curve already displaced by a polarization energy term (Fig. 12b.). The new form of the curve is assumed to be a Schottky image potential⁽¹⁶⁾ giving a square root dependence of Q , the resultant energy barrier, on F , the acting field. An equation for this model is;

$$Q = Q_o - (e^3 F)^{\frac{1}{2}} + \frac{1}{2} (\alpha_{atom} - \alpha_{ion}) F^2 \quad (16)$$

taking into account the difference in polarizabilities between atom and ion. Rewritten to allow evaporation of multiply charged ions:

$$Q = \lambda + \sum_n I_n - n\phi - (n^3 e^3 F)^{\frac{1}{2}} + \frac{1}{2} (\alpha_{atom} - \alpha_{ion}) F^2 \quad (17)$$

where $\sum_n I_n$ is the sum of the ionization potentials and $n e$ is the charge on the evaporating ion. Taking $Q = 0$ and neglecting the effects of polarizability, the field effect is balanced against the thermionic cycle to produce values for an evaporation field. If this is done for singly charged ions, the results are those incorporated in Table I using a unity subscript where applicable. Comparing these values to an image field for helium of $4.5 \text{ V}/\text{\AA}$ we see that a cutoff in image probability occurs at about the evaporation field of iron. In fact, Muller⁽¹⁸⁾ finds that helium can be used to image iron specimens but that the image is unstable, showing slow evaporation. Gases having a lower ionization potential can be used to stabilize the image but at the sacrifice of some intensity.

Another possibility, still using the image concept, is shown in Fig. 12c. Here ionization and evaporation occur coincidentally. The barrier in this case is the intersection of the atomic and ionic potential curves so that Q becomes a linear function of F for removal of the ion. Brandon suggests that sufficiently high fields will eliminate the Schottky hump on the ion potential curve so that the linear dependence would be expected⁽¹⁹⁾. He also introduces a correction factor having a linear dependence on F to include the effects of field penetration and a surface charge.

If Muller's equation obtaining the evaporation field for singly charged ions is rewritten for multiply charged ions;

$$(e^3 F_n)^{\frac{1}{2}} = (\lambda + \sum_n I_n - n\phi) n^{-\frac{3}{2}} = Q'_n \quad (18)$$

and given the conditions that Q'_n shall be a minimum, the values for F_n can be calculated. Table I is a listing of F_n for $n = 1, 2, 3$ for a number of elements. From this data one can predict the ion charge. But, as Brandon carefully points out⁽¹⁹⁾, the figures in parentheses are estimates of

unknown quality, and polarization effects have been neglected which, in some cases, determine the ion expectation. Indeed the evaporation field of $3.7 \text{ V}/\text{\AA}$ for tungsten, indicating a W^{+2} ion preference, is so far from the experimental data that even higher charges than those calculated might be expected. Furthermore, to effectively discuss the evaporating characteristics of any particular atom in an array it is necessary to consider i) variations in orientation, ii) variations in local geometry, and iii) variations in atomic species. This last point will govern image interpretations for the W-C alloys in this report.

Consider first two simple cases where a) the solute is more easily evaporated than the solvent, and then b) the solvent is more easily evaporated; in both cases, the solute concentration is assumed low, perhaps 1 or 2 atomic percent. In the first case, application of a field greater than that necessary to remove the solute but not high enough to disturb the solvent will, upon lowering the voltage for reimaging, leave behind a pitted surface. In the second case, reversing the circumstances of field adjustment, the reimaged surface is seen to be studded with lone atoms left behind as a plane of host atoms collapsed around it. In this instance, the remaining atoms must have withstood the more severe disturbance of having its planar neighbors wrested from it and later the increased field due to its singular protrusion. With higher solubilities the situation becomes more complex and the observed image contains a great deal of randomness in the location of enhanced sites.

For the particular case of tungsten and carbon, the solubility of carbon in tungsten is low, of the order of 0.1% at 2400°C ; and since the necessary evaporation field for carbon is considerably higher than that of tungsten, one would expect something like case b) previously mentioned. Two digressions from the simple theory come about as a result of the carbon

atom size. Its role as an interstitial in the bcc tungsten lattice quite probably limits its field enhancement behavior so that it cannot be seen against its host lattice image. Too, the high stress imposed on the tip by the electric field causes some expansion. Using an average bulk modulus for tungsten and the stress imposed at an assumed evaporation field for pure tungsten, $5.6 \text{ V}/\text{\AA}$, one arrives at an expansion of $\sim 4\%$. This would indicate a "super solubility" of carbon in tungsten, suppressing formation of a second phase. It is also expected that the nature of the carbon bond in the tungsten lattice would upset any simple picture. Gomer and Swanson have considered covalent, ionic, and intermediate types of bonding in their development of field desorption theory⁽¹⁷⁾, finding that the field dependence of the evaporation energy changes character completely with bond type.

" Muller has recently reported on a possible explanation for image points appearing in regular sequence but with a greater brightness than surrounding atoms⁽²⁰⁾. Using the coordination number of an atom in a given site as a direct indication of its electronic binding energy, he considers the case of an atom which moves to a position of lower bond coordination number but same bond type. A typical site is the edge of an atomic monolayer. This would be a field enhancement position which would mean greater depth of field penetration into the specimen. The increase in polarization binding energy associated with greater field penetration may be enough to offset the loss in electronic binding energy. If so, such a site would be "field stabilized". The increase in brightness is due to a reduction in X_c giving an increase in ionization probability and a contribution to the ion current from low hopping image gas atoms. On a clean tungsten image (see Fig. 3.) this would account for {001} zone decoration. This is a characteristic of

the metal and is temperature sensitive. Recalling the model by which an "under-the-surface" interstitial could create a field enhanced site, one would expect such a site to remain if an attempt was made to desorb the weaker bound surface contaminants. Such a case will be described in a later section.

3. Results:

3.1. Tungsten Carbon Alloy System

A portion of the tungsten-carbon phase diagram, reprinted from Hansen⁽³¹⁾, is given in Fig. 13. As indicated earlier the solubility of carbon in tungsten is low, ~0.1 At.% at 2475°C. Two compounds appear, both stoichiometric at low temperatures and one, W_2C , having a high temperature modification. Its low temperature α form is simple hexagonal with two tungsten atoms and one carbon atom per unit cell. Most probable cell dimensions are given as; $a = 2.994 \text{ \AA} \pm 0.002 \text{ \AA}$, $c = 4.724 \text{ \AA} \pm 0.002 \text{ \AA}$. The high temperature β modification gives an x-ray diagram similar to that of the α form except that several lines are missing. WC has a simple hexagonal structure previously reported as interpenetrating hex lattices of W and C⁽²¹⁾; but more recently the carbon atom has been found to assume the more specific 1/3, 2/3, 1/2 positions in the hexagonal tungsten structure^(22, 23, 24). Most probable cell spacings are; $a = 2.906 \text{ \AA} \pm 0.002 \text{ \AA}$, $c = 2.837 \text{ \AA} \pm 0.002 \text{ \AA}$. It has also been noted⁽²¹⁾ that the "c" axis of the W_2C lattice at higher temperatures decreases with increasing carbon content while the "a" dimension remains practically unchanged. Diffusion of tungsten in the WC structure is expected to be quite low as indicated by the high activation energy⁽³¹⁾; consequently, the appearance of the WC phase in a FIM image is expected to show sharp contrast with any previously observed structure.

The carbon concentration in each specimen depends on the technique by which the carbon was introduced. In each of the following methods certain basic steps were the same. Since the present microscope is not equipped for internal evaporation, it was necessary to image a clean tungsten specimen, record this image, remove the specimen from the microscope and place it in a separate vacuum chamber equipped for various deposition techniques, deposit the carbon, and return the specimen to the microscope for reimaging. Specimen orientation is easily established with stationary reference points allowing direct comparison of "before" and "after" photographs. Admittedly, contamination is a problem. Any material picked up by the surface during transfer of the specimen and not removed by pressure reduction in the evaporating system, stands the chance of being covered by the carbon deposit or of being diffused into the tungsten along with the carbon. Perhaps the most undesirable and most suspected contaminant is oxygen. Since weakly bound impurities accommodated on the specimen in the microscope without an applied field can be easily removed as demonstrated earlier, principal concern should be given to oxide formation. Here, however, we are assisted by the fact that tungsten oxide dissociates at 1700°C at atmospheric pressure. Consequently, the presence of the oxide is doubtful under normal operating conditions. This does not deny the presence of impurities. Easily evaporated atoms are removed from the surface during the reimaging process before any analysis is made of the structure. All interpretation is made on the basis of reactions of a pure tungsten specimen to the same type of "cleaning" operations.

Using the carbonizing method in which a cold specimen is rotated at a fixed distance from a continually evaporating carbon source, coverage over the specimen tip is uniform and the amount can be estimated by a color comparison technique applied to concurrent deposition on a smooth

porcelain surface. The color of deposited surface on a porcelain substrate is compared to standards where a fixed amount of carbon has been evaporated in the presence of similar substrates. This method is common to shadowing techniques for electron microscopy and has been shown to be quite accurate⁽³²⁾. A cold specimen so covered is replaced in the FIM where, at a pressure of $<10^{-6}$ mm Hg it is heated to $\sim 1500^{\circ}\text{C}$ for a penetration time which is dependent on the tip size and determined using bulk diffusion coefficients extrapolated from data presented by Kovenskii⁽²⁵⁾ and listed in Table II. For a penetration depth of 600 Å and a temperature of 1000°C , heating time is ~ 5 min. Since we are dealing with structures on an atomic level, these calculations are understandably crude. Moreover, the effect of any existing contaminants picked up by the specimen between imaging and carbonizing is ignored. For oxygen in particular, some justification for this exists in a report by Klein⁽²⁶⁾. He suggests that the disappearance of carbon evaporated on clean tungsten with an over-layer of oxygen applied is due to oxidation of carbon which occurs at a substantial rate within his operating temperature range (1000°K to 1200°K). In this experiment some carbon oxidation is expected to take place and in the presence of excess carbon the trapped oxidation products lead to cracking of the surface layer. This is suggested by the dark lines crossing the images in various directions. Residual untrapped surface contamination can be removed in the microscope by heating and evaporating.

If the carbon was deposited on a heated tungsten specimen, the calculations are accurate insofar as they apply to a one sided deposition. As shown in Fig. 14., proper coverage is obtained by evaporation ahead of the specimen. Indeed, our model for determining specimen coverage is most closely approximated by placing the carbon source directly in front of the tip. Here, however, as in any fixed specimen position instance, surface diffusion is competing with volume diffusion and the accuracy of

the carbon concentration is difficult to estimate. The following sections are divided as alloys according to a maximum carbon content as calculated from the deposition model.

3.2. Tungsten-8At.% Carbon

Fig. 15a. through f. demonstrates carbonizing followed by a diffusion treatment in the microscope. Fig. 15a. is the clean tungsten image in typical [110] orientation, slightly off center so that three other {110} type poles can be seen. During the heat treating process, the specimen changed position slightly, so for this particular set no attempt has been made to align the photographs with reference to pole positions. The orientation of each picture as a whole relative to the ones before and after and to the fixed screen is the same, however. Fig. 15b. is not quite the cold deposit as it has been heated to $\sim 600^{\circ}\text{C}$ for outgassing purposes. Between Figs. 15b. and c. and between c. and d. the specimen was heated to $\sim 1500^{\circ}\text{C}$ in a two second burst. This temperature is high enough to promote oxidation of the carbon and the result is a series of random dark line surface cracks. Both the first and second heating bursts show removal of larger areas of the surface layer, the second not as effective as the first. A few scattered regions exist where the ringed appearance of stacked atomic planes is distinguishable from the background. These rings do not necessarily represent the tungsten structure in that they may be only an oriented overgrowth. Each of the images was quite stable except near the outer rim of the screen where an occasional scintillating pattern was observed, typical of contaminants evaporating under the high field. In Fig. 15e., a large break in the surface structure appeared after a light flash, giving warning that the tip was breaking up. A larger exposed surface area lowered the field and allowed existing impurities to become

stable. Raising the voltage caused another section to break off leaving only a few areas above and the left of center where the ring structure remained visible. Shortly after the last photograph was taken, the specimen yielded to the field applied stress.

The specimen shown in Figs. 16a. through f. is asymmetrical, having a blunted chisel shape and therefore pronounced ionization probability over the ridge. These pictures like all others hold the image in a fixed position as shown by the pole indices. While the calculated carbon content has not changed, treatment of this specimen was changed to promote carbide formation. As before, carbon was cold deposited but heated in the microscope at a pressure of $<10^{-6}$ mm Hg to $\sim 1200^\circ\text{C}$ for 15 minutes before imaging. Carbon penetration at this temperature seems a great deal less than that calculated indicating thermal stability of the carbon layer as suggested by Klein for the low temperature region⁽²⁶⁾. Otherwise, the specimen responded to the treatment as expected forming patches of a strongly oriented overlayer suggestive of carbide formation (Fig. 16b.). By field evaporation it was possible to remove the overlayer and reveal a scattering of lesser impurities and the insoluble carbon (Fig. 16c). Raising the voltage in a pulse fashion by $\sim 50\%$ of its image value evaporated most of the loosely bound surface atoms revealing a near normal tungsten image. (Fig. 16d.). Layer edges do appear ragged after this treatment and this is attributed to carbon in solution. Turning off the voltage and momentarily heating the specimen to $\sim 1500^\circ\text{C}$, produced the image in Fig. 16e. This treatment was expected to bring carbon to the surface in addition to freely contaminating the specimen. Subsequent cleaning by field evaporation gave the less disturbed pattern of Fig. 16f.

3.3 Tungsten-16At.% Carbon

Fig. 17 shows the results of the first attempt carburizing. The run was not as successful as we had hoped since the specimen deformed during an outgassing treatment in the microscope, the central pole sliding off to the right as seen in a comparison of the clean tungsten picture (Fig. 17a.) and the first picture of the carburized specimen (Fig. 17b). A sharp ridge near the specimen shank moved into the field of view from the left providing a sharp but shallow point on which imaging could take place. When the voltage was raised over a normal evaporation level, dark lines appeared as in Fig. 17c. Further evaporation indicated these were slip bands about 50 Å wide extending across the crystal and following the ridge contour. Slip bands are identified by the manner in which they were produced, their appearance in following the contour of the specimen ridge, and the depth of their existence in the specimen. Figs. 17c., d., e., and f., show successive stages during the evaporation revealing apparent motion of the bands to the right. This phenomenon is a result of following the bands' positions in the crystal by removal of surface layers. In each of the last three pictures clustering occurs over the length of each dark band. This could be due to surface contaminants or displaced tungsten atoms where buried impurities seek a more open structure at the band edge.

3.4. Tungsten-48At.% Carbon

A second attempt at carburizing the tungsten in one step produced results similar to some discussed earlier (see Tungsten-8At.% Carbon; second series). Temperature of the specimen during carburization was kept at $\sim 1500^{\circ}\text{C}$. An arrow in the upper left corner of Fig. 18b. indicates the direction in which carbon was cast onto the tungsten. Just to the right of the arrow in the same figure an almost rectangular shaped plane

of atoms appears. This is one of the most obvious indications of over-growth strongly suggesting the presence of carbides. Following a diagonal from this point down and to the left, two more planes are found closely attached and not quite coincident with the underlying tungsten lattice. The appearance of pole indices in this and the following figure does not mean that the planes represented are pure tungsten; they are simply intended to align the images before and after carburization. Some field evaporation removed the outer layers of the planes just mentioned (Fig. 18c.), ultimately wearing away the entire outer layer and exposing a surface of insoluble impurities (Fig. 18d.). Heating the tip to $\sim 1500^{\circ}\text{C}$ for 10 sec, and cleaning the surface with the field produced the more developed image shown in Fig. 18e. Continued evaporation revealed the original tungsten structure emerging in correct orientation although cluttered with impurities which are probably an indication of carbon solubility (Fig. 18f. and g.).

4. Discussion:

Since theories with which the field ion microscope is connected are continually being revised and extended, we will limit discussion to the tungsten-carbon alloy system and the possibilities stemming from a search of this system with the microscope. At a glance the tungsten-carbon phase diagram appears rather simple, having only two known compounds both having virtually no solubility spread. The bcc tungsten lattice itself accepts only a small amount of carbon. These facts imply that the FIM image for a carbide or the saturated tungsten lattice would be completely coherent. That this has not been the case in the experiments run thus far, is an indication of the rapidity and ease with which a surface becomes contaminated. To distinguish the effects of carbon on tungsten from contaminants normally present, diffusion will have to be done in ultra-high

vacuum. The relatively low dissociation temperature of tungsten oxide assists decontamination. Having once minimized this problem, the field ion microscope can be used to observe almost any physical disturbance produced by carbon in the tungsten lattice. Clustering at slip bands has been shown. Grain boundaries are not common to FIM work because of limitations on the field of view but they have been observed and recorded on several occasions^(10, 11, 12, 17, 18) and would provide sites where clustering might be expected.

Calculations concerning the depth of carbon penetration are high by about one order of magnitude at 1000°C but this is quite probably due to extrapolation of high temperature diffusion data over a low temperature range. Examination of specimens in which diffusion took place only 500°C higher sometimes exceeded the range of the power supply before field evaporation was able to reproduce the original tungsten structure in great detail. Difficulties in calculating carbon content are inherent in that all figures must be obtained from deposits except in the "parts per million" category where direct counting from the image may be possible. Even this is doubtful since under present theories the carbon interstitial is not expected to stand out against the tungsten background. One can then only improve the model for deposition and maintain more rigid control over the amount evaporated or deposited until errors involved become negligible with respect to estimates of surface coverage.

The existence of some form of a carbide appears to have been established by observance of a regular arrangement of surface atoms not in direct correlation with the known underlying tungsten substrate. The nature of this overlying structure has yet to be established, but it does seem to have a relation to the tungsten substructure even though separated from it by a scattering of impurities. This might be expected since impurities would be filling in holes where the individual structures did

not have one on one coincidence. Stresses due to the electric field favor solubility of carbon and the presence of even a monolayer of oxygen leads to oxidation of carbon and associated surface cracking. As a result, the overgrowth layers observed so far have been patchy with no well defined boundaries. There is a good chance for improvement here since the field effect is low and may not be too important and oxidation can be controlled.

5. Summary:

A field ion microscope examination of the tungsten-carbon alloy system promises new and useful information not yet available by other means. There are limitations, both theoretical and practical. The most obvious ones at present are:

- 1) The carbon interstitial according to present belief should not be visible against a tungsten background.
- 2) Oxidation of carbon disrupts the surface structure.
- 3) Tungsten becomes extremely brittle after heating over $\sim 1000^{\circ}\text{C}$ making a cold work study difficult.
- 4) High temperature diffusion studies are prohibited by excessive blunting of the specimen.

The advantages and attractive possibilities, however, far outweigh these limitations. Some questions involving the carbides have only recently been answered and by indirect statistical means. Unless structural limitations are more severe than they appear the field ion microscope will give a clearer picture than has been observed to date.

REFERENCES

1. Muller, E. W., *J. Appl. Phys.*, 27, 474 (1956)
2. Muller, E. W., *Physik Z.*, 37, 838 (1936)
3. Muller, E. W., *Adv. in Elect. and Electron Physics*, 13, 83 (1960)
4. Gomer, R., "Field Emission and Field Ionization", Harvard Press, Cambridge, 1961
5. Brenner, S. S., "Metal Surfaces", ch. 10, ASM, Metals Park, O., 1963
6. Waclawski, B. J. and Muller, E. W., *J. Appl. Phys.* 32, 1472 (1961)
7. McLane, S. B., Muller, E. W., and Nishikawa, O., *Rev. Sci. Instr.*, 35, 1297 (1964)
8. Feldman, U. and Gomer, R., *J. Appl. Phys.*, 37, 2380 (1966)
9. Good, R. H. and Muller, E. W., *Handbuch der Physik*, Springer, Berlin, 21, 176 (1956)
10. Brandon, D. G., Ralph, B., Ranganathan, S., Wald, M. S., *Acta Met.*, 12, 813 (1964)
11. Hren, J., *Acta Met.*, 13, 479 (1965)
12. Ryan, H. F. and Suiter, J., *Acta Met.*, 14, 847 (1966)
13. Muller, E. W., "Imperfections in Crystals", p. 77, Eds. J. B. Newkirk and J. H. Wernick, Interscience Publishers, N. Y., 1961
14. Ranganathan, S., Bowkett, K. M., Hren, J., Ralph, B., *Phil. Mag.*, 12, 841 (1965)
15. Brandon, D. G., *Phil Mag.*, 13, 1085 (1966)
16. Muller, E. W., *Phys. Rev.*, 102, 618 (1956)
17. Gomer, R. and Swanson, L. W., *J. Chem Phys.*, 38, 1613 (1963)
18. Muller, E. W., *J. Appl. Phys.*, 30, 1843 (1959)
19. Brandon, D. G., *Surface Science*, 3, 1 (1965)
20. Muller, E. W., *Surface Science*, 2, 484 (1964)
21. Hansen, M., "Constitution of Binary Alloys", McGraw-Hill, N. Y., (1958)

22. Butorina, L. N., Soviet Phys. Cryst., 5(2), 216 (1960)
23. Leciejewicz, J., Acta Cryst., 14, 200 (1961)
24. Parthé, E. and Sadogopan, V., Monatshefte Chem., 93, 263 (1962)
25. Kovenskii, I. I., "Diffusion in Body-Centered Cubic Metals", ch. 22, ASM, Metals Park, O., 1965
26. Klein, R., J. Chem. Phys., 21, 1177 (1953)
27. Ryan, H. F. and Suiter, J., Phil. Mag., 10, 727 (1964)
28. " Muller, E. W., Acta Met., 6, 620 (1958)
29. Ralph, B. and Sounhon, M. J., Science Jour., 2 (2), 50 (1966)
30. " Muller, E. W., from "Reactivity of Solids", Eds. J. H. DeBoer et al, Elsevier Publ. Co., Amsterdam, 1960
31. Baskin, M. L., Tret'yakov, V. I., Chaprova, I. N., Phys. of Metals and Metallography, 14, #3, 86 (1962)
32. Kay, D., "Techniques for Electron Microscopy", Blackwell, Oxford, 1961

Acknowledgements

We wish to thank Professor B. Roessler for his helpful suggestions during the experimental phase of this work. Our gratitude is extended to the Advanced Research Projects Agency for financing establishment of the microscope facility under contract ARPA SD86.

Table I

-1A-

Z	Element	ϕ (ev)	λ (ev)	$\Sigma_{n=1}^{\infty}$ (ev)	$\Sigma_{n=2}^{\infty}$ (ev)	$\Sigma_{n=3}^{\infty}$ (ev)	Q_1' (ev)	Q_2' (ev)	Q_3' (ev)	F_1^{∞} V/A	F_2^{∞} V/A	F_3^{∞} V/A	Ion expected
4	Be	3.92	3.45	9.32	27.5	181	8.87	8.15	33.2	5.4	4.6	76.0	Be ²⁺
5	B	4.6	5.98	8.28	33.4	71	9.66	11.6	12.2	6.5	9.3	10.1	B ⁺
6	C	4.34	7.40	11.3	36.1	84	14.3	10.9	15.1	14.3	8.2	15.8	C ²⁺
12	Mg	3.70	1.52	7.64	22.4	102	5.46	5.85	17.7	2.1	2.4	21.7	Mg ²⁺
13	Al	4.20	3.30	5.97	24.8	53.3	5.07	6.96	8.5	1.8	3.4	5.0	Al ⁺
14	Si	4.80	4.90	8.15	24.5	58.0	8.25	7.0	9.28	4.7	3.4	6.0	Si ²⁺
20	Ca	3.20	1.99	6.11	18.0	62.0	4.90	4.80	11.8	1.7	1.6	9.7	Ca ²⁺
22	Ti	4.17	4.85	6.83	20.4	48.0	7.51	5.8	7.4	4.0	2.3	3.8	Ti ²⁺
23	V	4.4	5.30	6.74	20.8	47.3	7.64	6.1	7.6	4.1	2.6	4.0	V ²⁺
24	Cr	4.45	4.16	6.74	23.4	55.1	6.74	6.68	8.9	3.15	3.1	(5.5)	Cr ²⁺
25	Mn	3.95	2.82	7.43	23.1	57.1	6.30	6.35	(9.4)	2.75	2.8	(6.1)	Mn ²⁺
26	Fe	4.17	4.13	7.90	24.4	54	8.00	7.19	8.83	4.5	3.6	5.4	Fe ²⁺
27	Co	4.40	4.40	7.86	25.5	59	7.86	7.35	(9.6)	4.3	3.7	(6.4)	Co ²⁺
28	Ni	5.01	4.36	7.63	25.8	62.1	7.08	9.15	(9.9)	3.5	3.5	(6.8)	Ni ²⁺
29	Cu	4.55	3.50	7.72	27.9	66	6.67	7.90	(11)	3.1	4.3	8.1	Cu ⁺

Table I (contd.,)

Z	Element	ϕ (ev)	λ (ev)	ξ			ξ			ξ			ξ			Ion Zn^{2+}
				$n=1$ (ev)	$n=2$ (ev)	$n=3$ (ev)	$n=1$ (ev)	$n=2$ (ev)	$n=3$ (ev)	Q_1 (ev)	Q_2 (ev)	Q_3 (ev)	F_1 V/ \AA	F_2 V/ \AA	F_3 V/ \AA	
30	Zn	4.31	1.36	9.39	27.4	67.4	6.44	7.10	10.7	2.9	3.5	7.9				
31	Ga	4.16	2.88	5.97	26.5	57.3	4.74	7.2	9.2	1.6	3.6	5.8				
32	Ge	4.80	3.97	7.88	24.0	58.1	7.05	6.50	9.15	3.5	2.9	5.8				
40	Zr	4.12	6.33	6.84	20.8	44.9	9.05	6.67	7.47	5.7	3.1	3.8				
41	Nb	4.01	6.87	6.88	(20)	(45)	9.74	(6.6)	(8.0)	9.7	(3.0)	(4.4)				
42	Mo	4.30	6.15	7.13	(21)	(48)	8.98	(6.6)	(8.1)	6.5	(3.0)	(4.5)				
44	Ru	4.52	5.52	7.36	(23)	(52)	8.36	(7.1)	(8.6)	4.9	(3.5)	(5.1)				
45	Rh	4.80	5.77	7.46	(26)	(56)	8.43	(7.6)	(9.1)	5.0	(4.0)	(5.7)				
46	Pd	4.99	4.08	8.33	(28)	(61)	7.42	(7.8)	(9.7)	3.8	(4.2)	(6.5)				
47	Ag	4.70	2.90	7.58	29.0	64.9	5.78	7.96	10.3	2.3	4.4	7.3				
48	Cd	4.04	1.16	8.99	25.9	64	6.12	6.70	10.2	2.6	3.1	7.2				
50	Sn	4.39	3.17	7.30	21.9	52.6	6.08	5.75	8.2	2.55	2.3	4.7				
57	La	3.3	4.33	6.51	17.9	37.0	6.64	5.50	6.03	3.1	2.1	2.5				
73	Ta	4.20	8.25	7.7	(21)	(43)	11.7	(7.4)	(7.4)	9.3	(3.8)	(3.8)				
74	W	4.52	8.67	7.98	(21)	(45)	12.1	(7.3)	(7.9)	10.2	(3.7)	(4.3)				

Table F (contd.)

Z Element	ϕ (ev)	λ (ev)	Σ n=1			Σ n=2			Σ n=3			Σ n=4			F ₁ (ev)	F ₂ (ev)	F ₃ (ev)	Ion
			Q ₁ (ev)	Q ₂ (ev)	Q ₃ (ev)	Q ₁ (ev)	Q ₂ (ev)	Q ₃ (ev)	Q ₁ (ev)	Q ₂ (ev)	Q ₃ (ev)	Q ₁ (ev)	Q ₂ (ev)	Q ₃ (ev)				
75 Re	5.1	8.30	7.87	(21)	(47)	11.1	(6.7)	(7.6)	8.2	(3.1)	(4.0)					Re ²⁺		
76 Os	4.55	6.95	8.7	(24)	(49)	11.1	(7.8)	(8.4)	8.5	(4.2)	(4.9)					Os ²⁺		
77 Ir	5.0	6.50	9.2	(25)	(52)	10.7	(7.6)	(8.8)	7.9	(4.0)	(5.4)					Ir ²⁺		
78 Pt	5.32	5.62	8.96	27.5	(56)	9.26	7.7	(8.8)	6.3	4.1	(5.4)					Pt ²⁺		
79 Au	4.82	3.67	9.22	29.2	(59)	8.10	8.20	(9.4)	4.5	4.3	(6.1)					Au ²⁺		
80 Hg	4.52	0.64	10.4	29.2	53.2	6.51	7.35	7.75	2.9	3.7	4.2					Hg ⁺		
81 Tl	4.05	1.87	6.12	26.4	56.2	3.94	7.14	8.85	1.1	3.5	5.4					Tl ⁺		
82 Pb	4.04	2.03	7.42	22.4	54.3	5.41	5.78	8.50	2.0	2.3	5.0					Pb ²⁺		
83 Bi	4.34	2.15	(8.8)	(26)	(53)	(6.6)	(6.9)	(8.1)	(3.0)	(3.3)	(4.5)					Bi ²⁺		
90 Th	3.35	6.30	4.74	?	?	7.69	?	?	4.1	?	?					Th [?]		
92 U	3.27	5.02	6.0	?	?	7.75	?	?	4.2	?	?					U [?]		

Adapted from Brandon (19)

Table II

<u>Temp., °C</u>	<u>D, cm^2/sec</u>
1800	5.02×10^{-7}
1850	5.49×10^{-7}
1900	7.24×10^{-7}
2000	1.17×10^{-6}
2100	1.77×10^{-6}
2200	2.75×10^{-6}
2300	3.15×10^{-6}
2400	4.51×10^{-6}
2500	5.87×10^{-6}
2600	8.74×10^{-6}
2700	1.12×10^{-5}
2800	1.41×10^{-5}

$$D_0 = 9.22 \times 10^{-3} \text{ cm}^2/\text{sec}$$

$$E = 40.4 \text{ k cal/mole}$$

Diffusion Coefficient Data for Carbon in Tungsten.

Adapted from Kovenskii⁽²⁵⁾.

List of Figures

1. FIM image tube with cold finger inserted.
2. FIM mounted on pumping station.
3. Ionization of the image gas at the tip surface.
4. Tungsten image, {110} orientation.
5. Field effect on ionization of a hydrogen atom near a tungsten surface.
6. Thermal scattering of ions.
7. Dependence of resolution on equi-potential spheres.
8. Tungsten bicrystal.
9. Cross-sectional sketch of tungsten bicrystal.
10. Effect of interstitials on an atomic surface.
11. Adsorption and desorption applied to tungsten.
12. Field effect on the potential well.
13. A partial tungsten-carbon phase diagram.
14. Dependence of deposit coverage on source location.
15. Tungsten-8At.% carbon ion micrographs (first series).
16. Tungsten-8At.% carbon ion micrographs (second series).
17. Tungsten-16At.% carbon ion micrographs.
18. Tungsten-48At.% carbon ion micrographs.

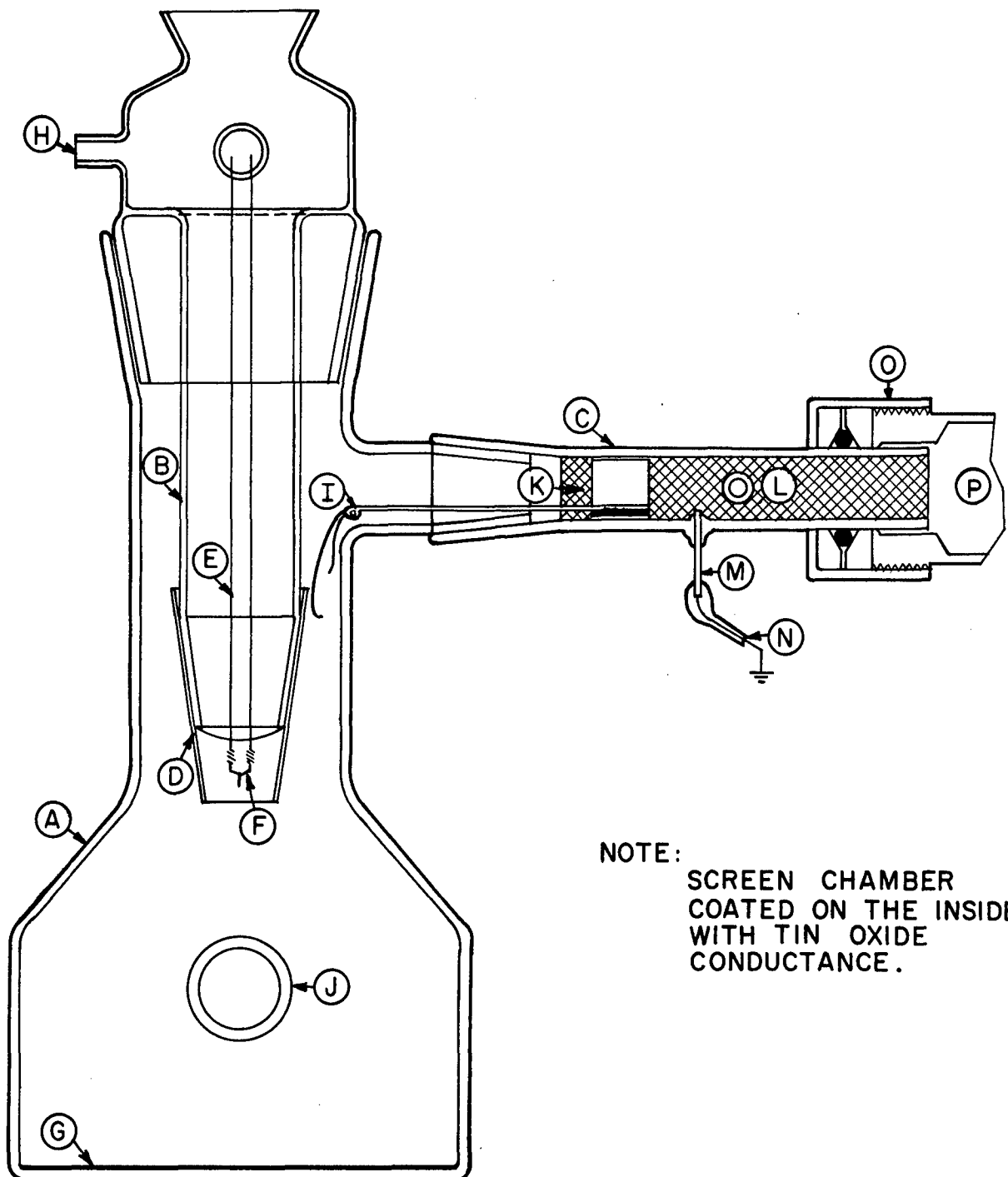
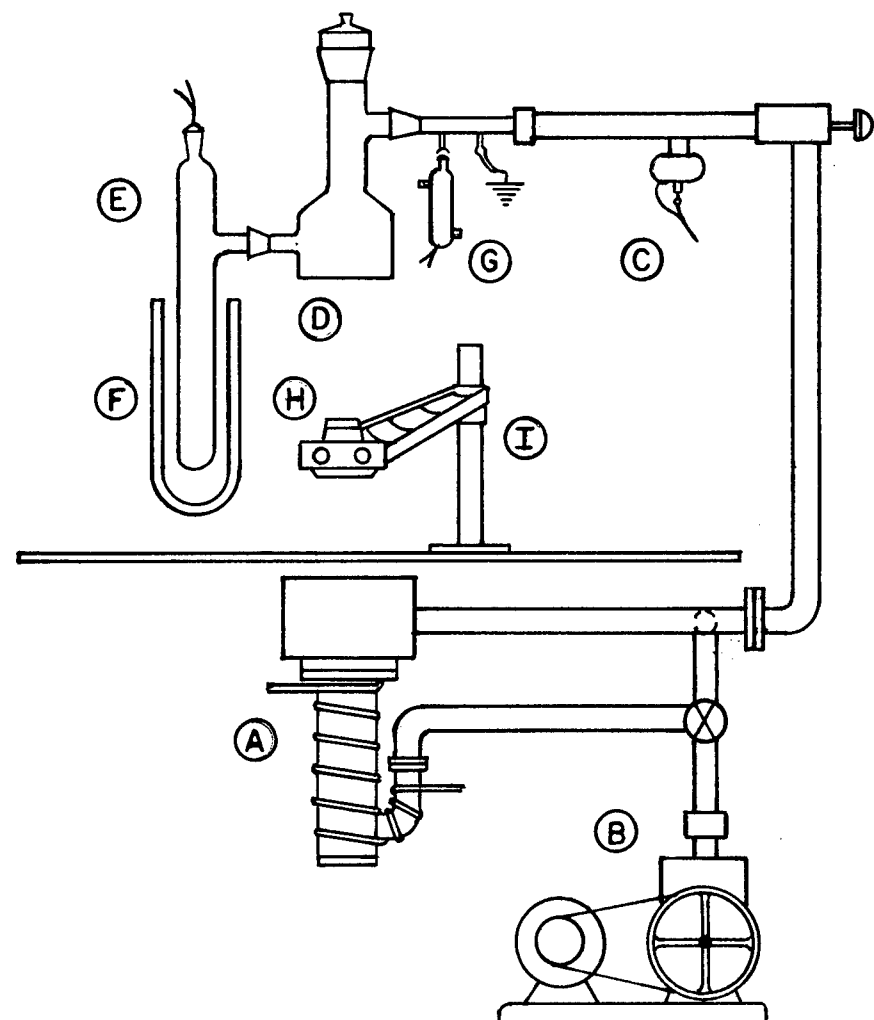


Figure 1. FIM image tube with cold finger inserted shown connected to the diffusion pump line. A key for this figure is on the following page.

Figure 1. Key

- A. Screen chamber
- B. Cold finger
- C. Connecting tube
- D. Aluminum cone
- E. Tungsten leads
- F. Specimen
- G. Phosphor screen
- H. Hose connection
- I. Spring wire ground strap
- J. Getter tube outlet
- K. Aluminum coating
- L. Image gas inlet
- M. Tungsten grounding lug
- N. Ground cable
- O. Compression seal
- P. Diffusion pump connection

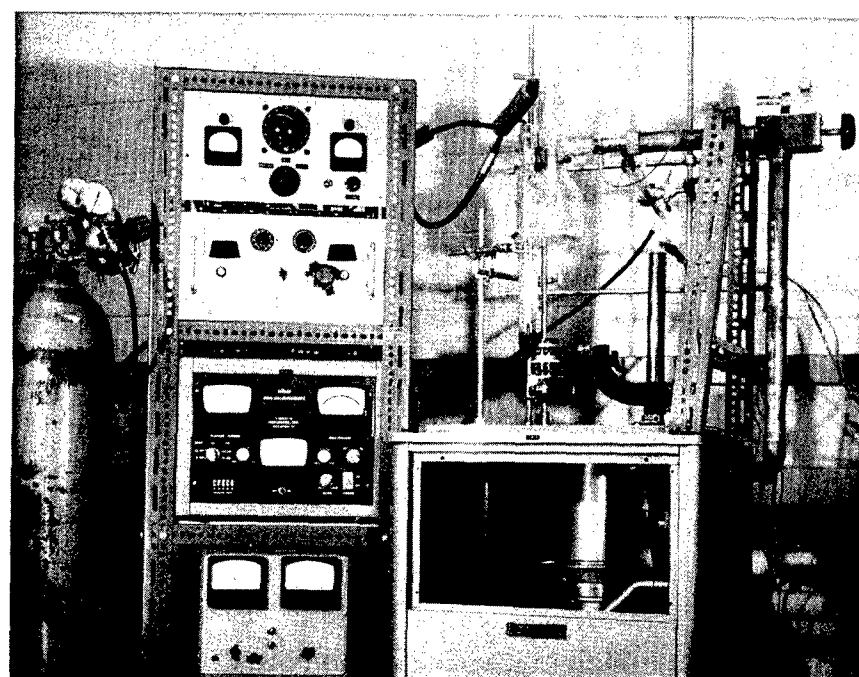


D

Figure 2. a.) FIM mounted on pumping station. b.) FIM unit with power supply connected. A key for this figure is on the following page.

Figure 2. Key

- A. 3" oil diffusion pump
- B. Mechanical fore and roughing pump
- C. NRC model 524 cold cathode vacuum gage tube
- D. Screen chamber
- E. Getter tube
- F. Liquid Nitrogen dewar
- G. Quartz Helium diffuser
- H. Camera
- I. Swing-away camera mount with locking ring



b

FIG. 2

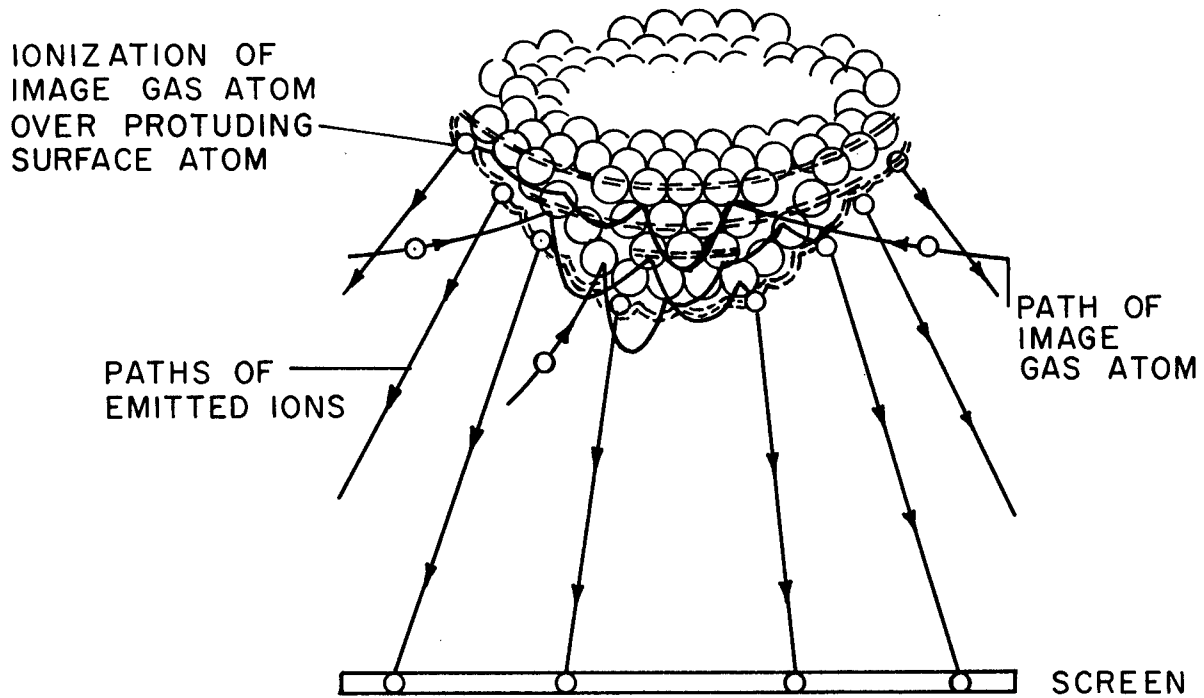


Figure 3. Atomic view of the specimen tip. Image gas dipole is drawn to repeated collisions with the metal surface until escape or ionization takes place. From Brandon and Southen⁽²⁹⁾.

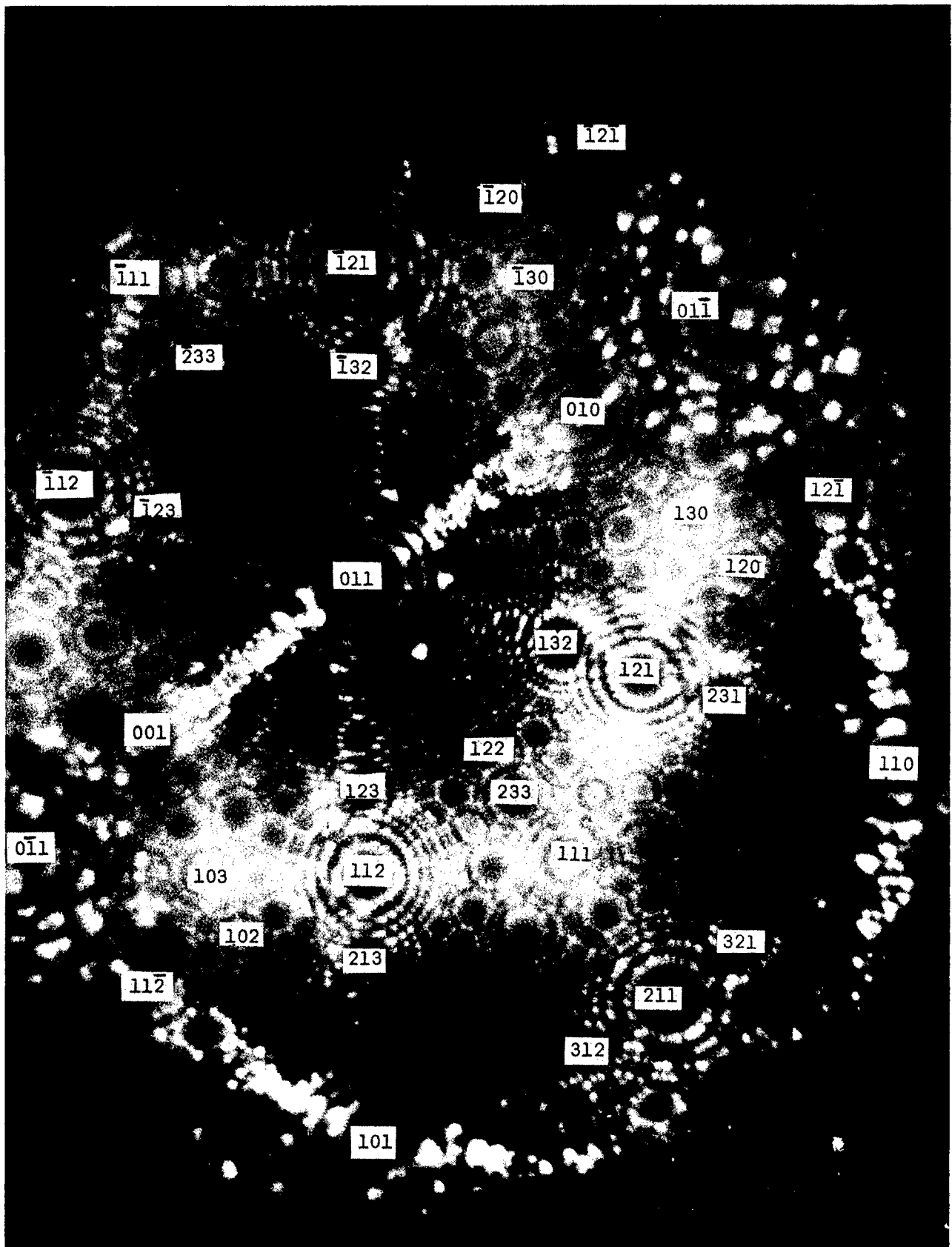


Figure 4. Tungsten image, {110} orientation, 10,000 V 77°K. Specimen radius $\sim 630\text{\AA}$. X100 818

ABERDEEN PROVING GROUND, MD.
STEAM-TH.

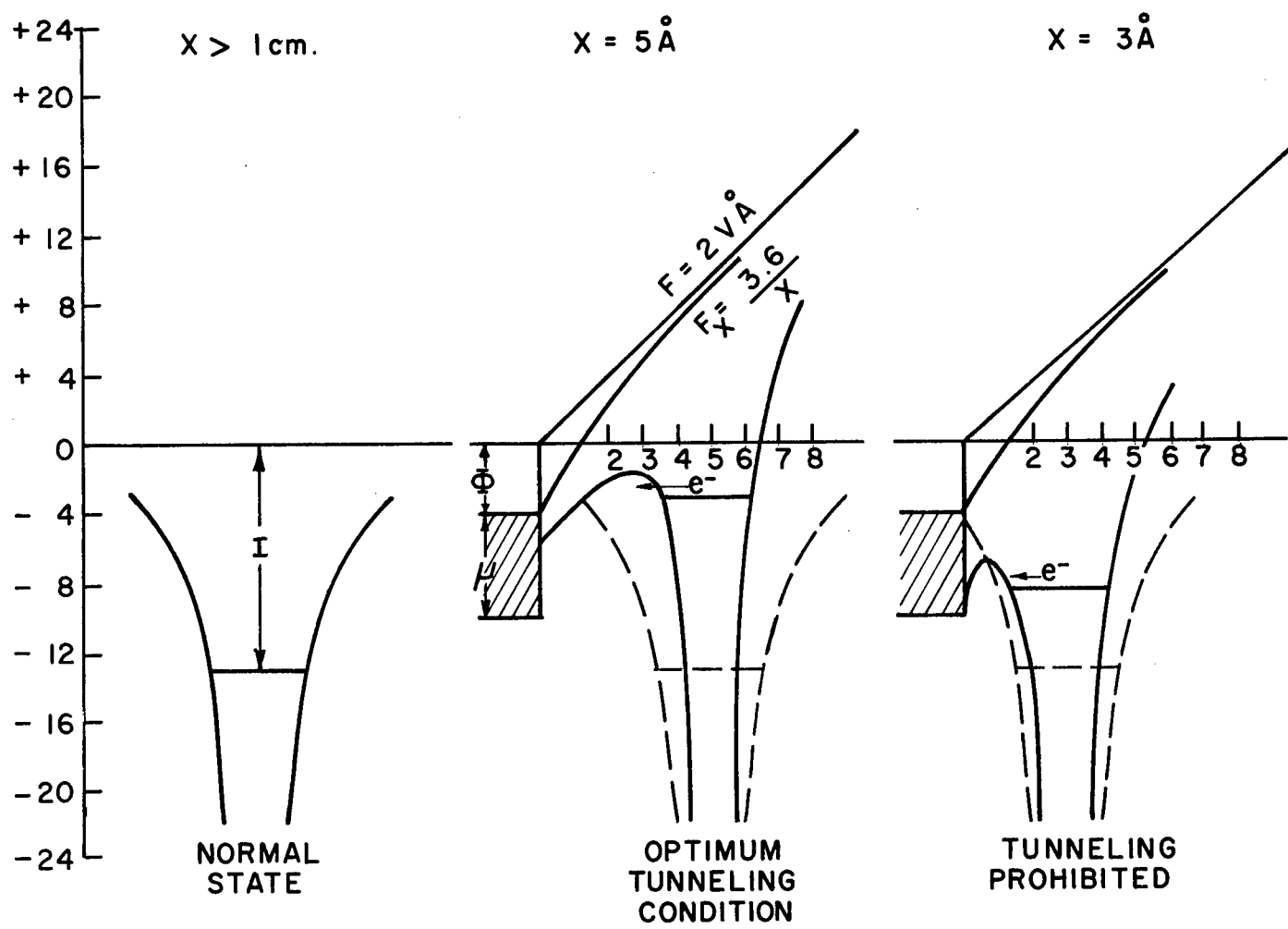


Figure 5. Ionization of a hydrogen atom near a tungsten surface in a field of $2V/\text{\AA}$. X is the distance from the metal surface. From Brenner(5).

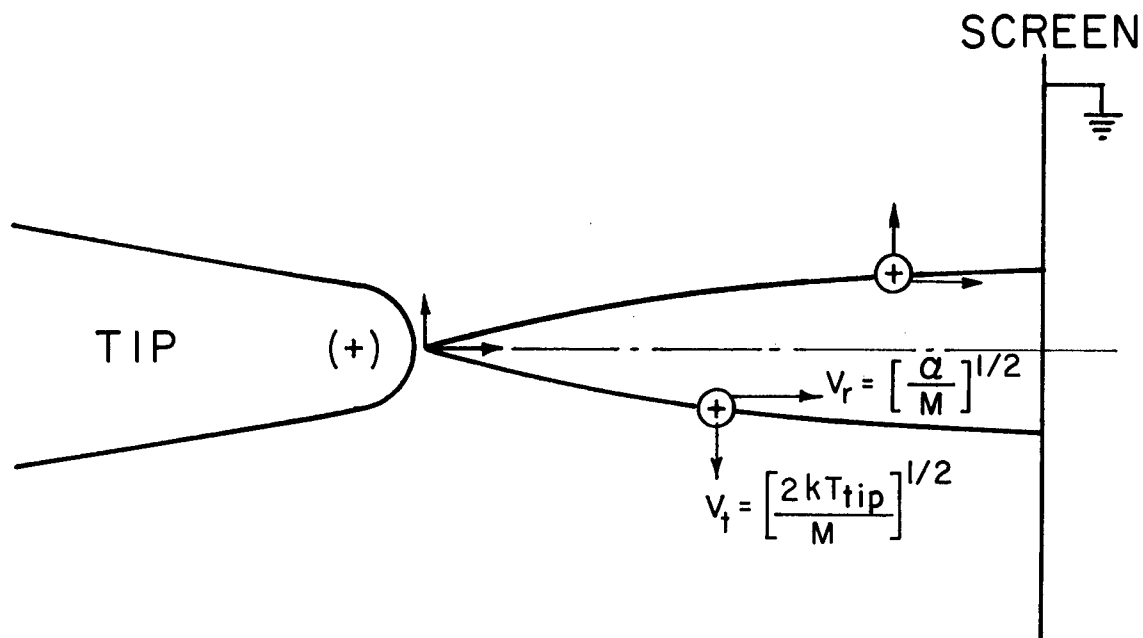


Figure 6. A scattering disk appears on the screen as a result of a thermal velocity imparted to the ions at the tip.

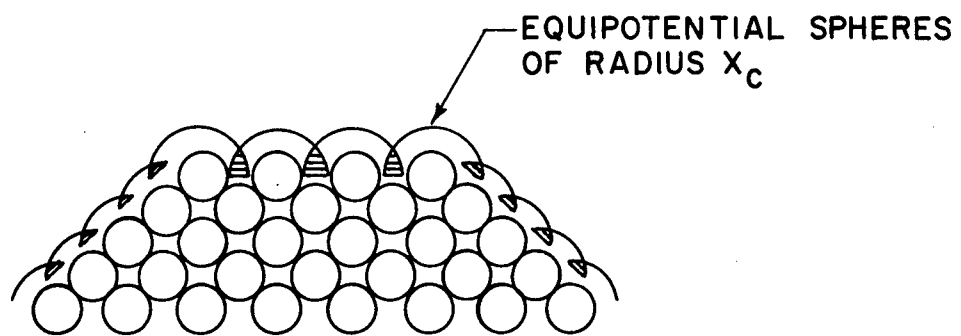
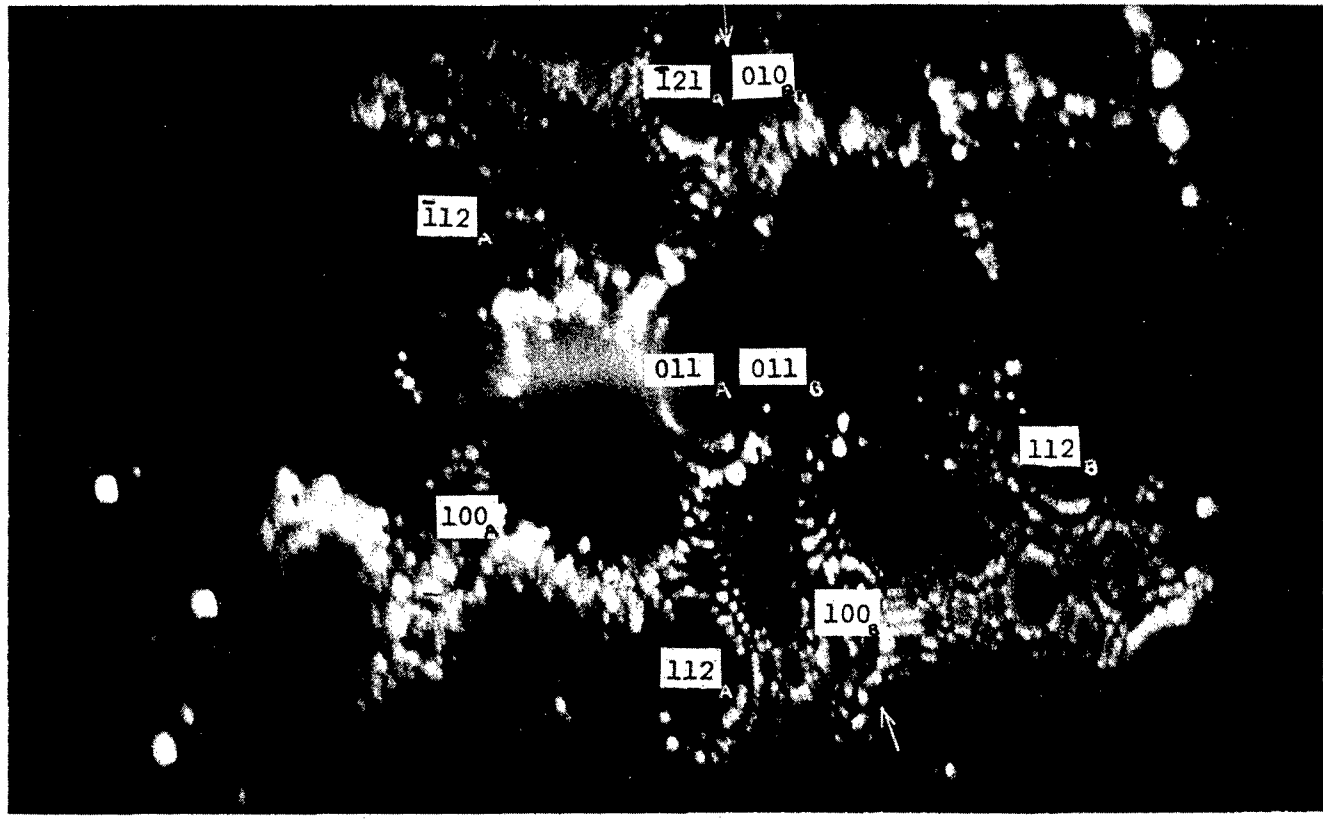
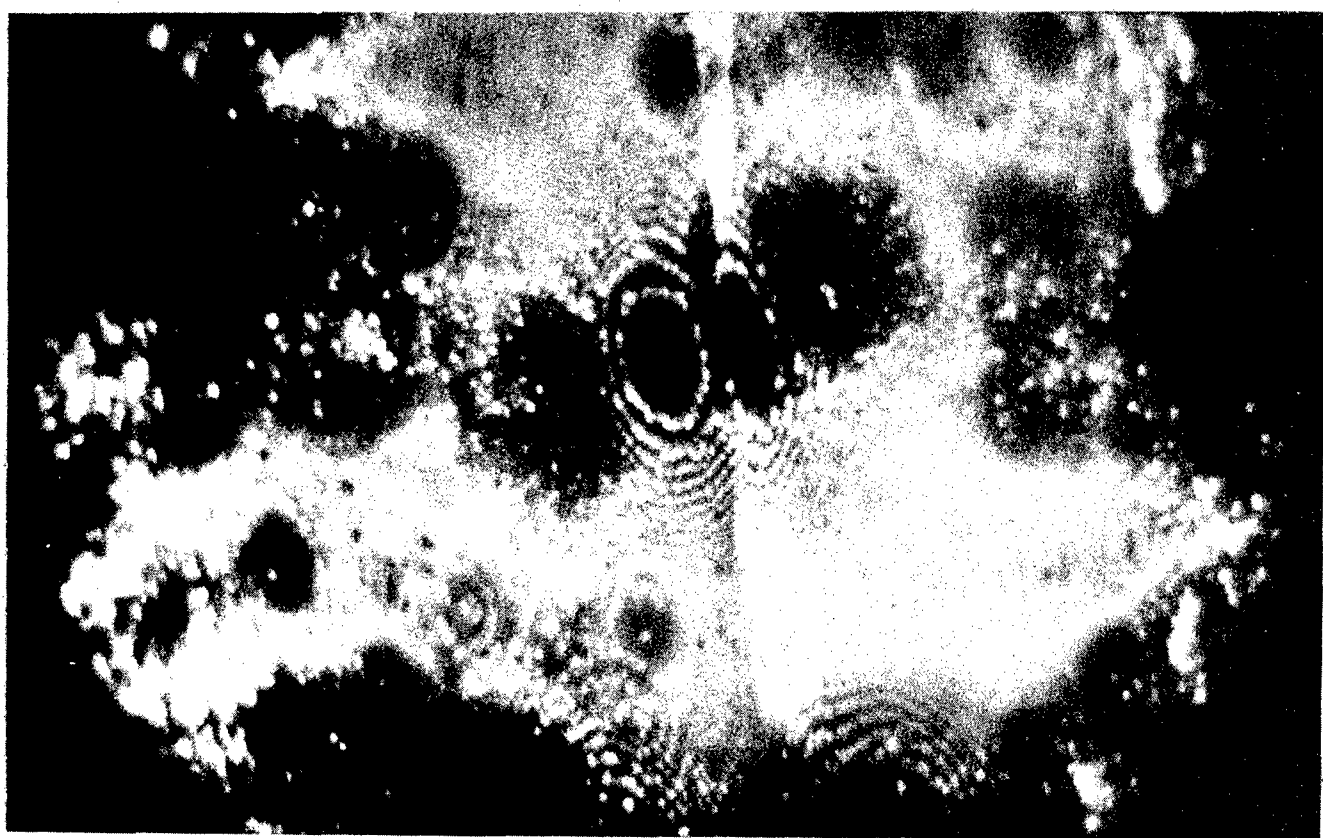


Figure 7. Specimen cross section showing that resolution is dependent on overlap of equi-potential "spheres". Less overlap gives better resolution.



D



b

Figure 8. a.) Tungsten bicrystal; 18,200V 77°K; $r_A = 270\text{\AA}$, $r_B = 580\text{\AA}$, plane of the boundary is $\{001\}$ type. b.) same tip at 20,500V showing boundary position by increasing the local field perturbation.

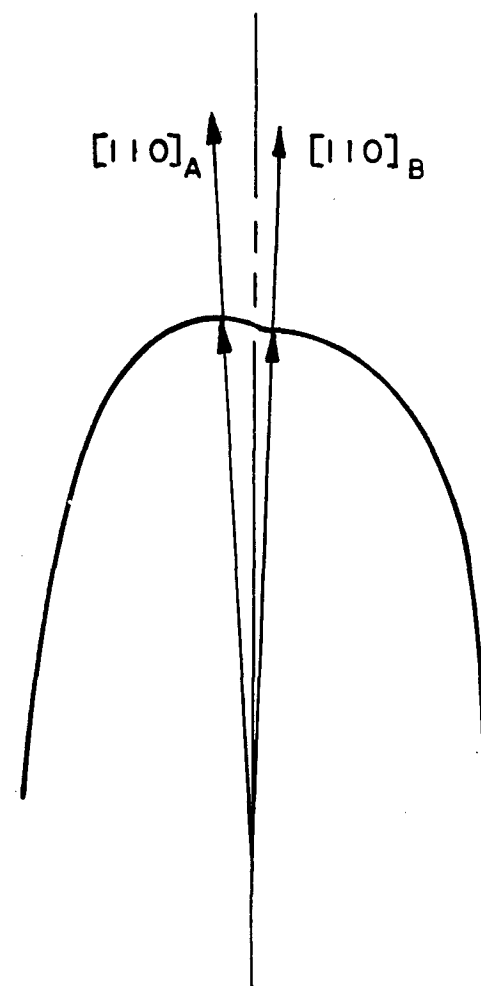


Figure 9. Cross sectional sketch of tip containing tungsten bicrystal of Figure 8.

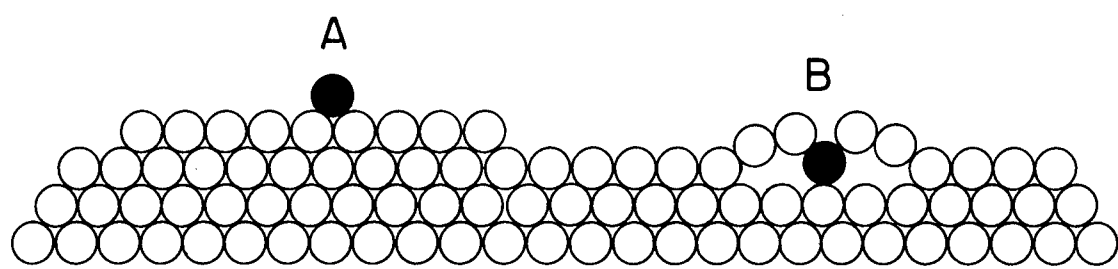
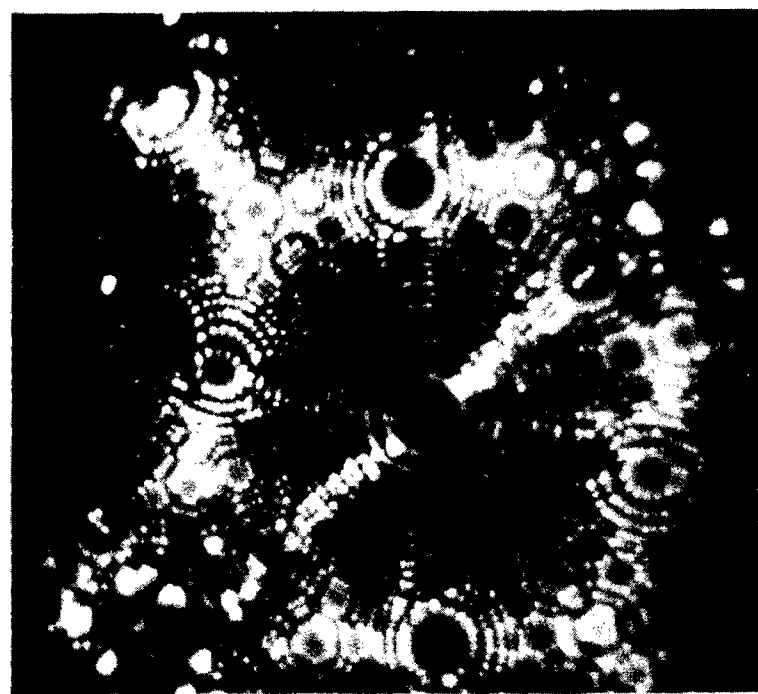
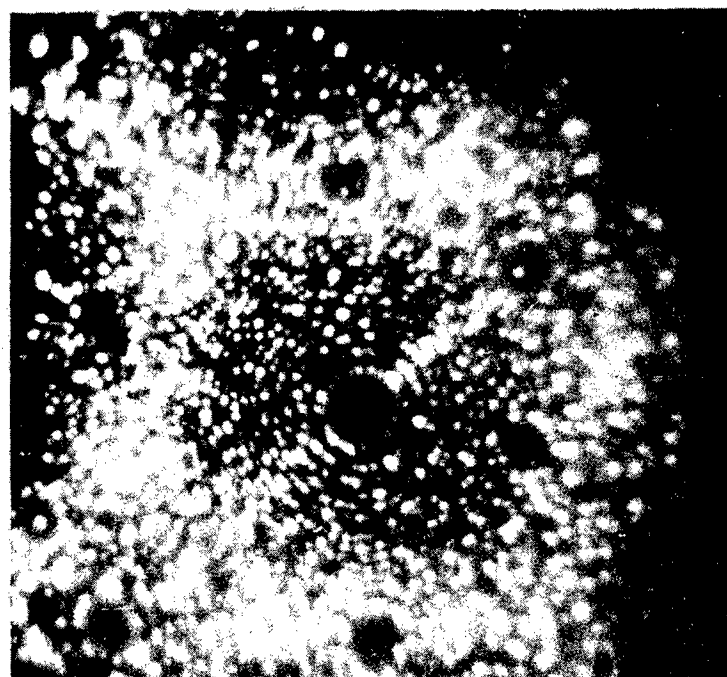


Figure 10. Cross section of four atom layers showing displaced surface atom at A and an interstitial bulging out the surface layer at B.

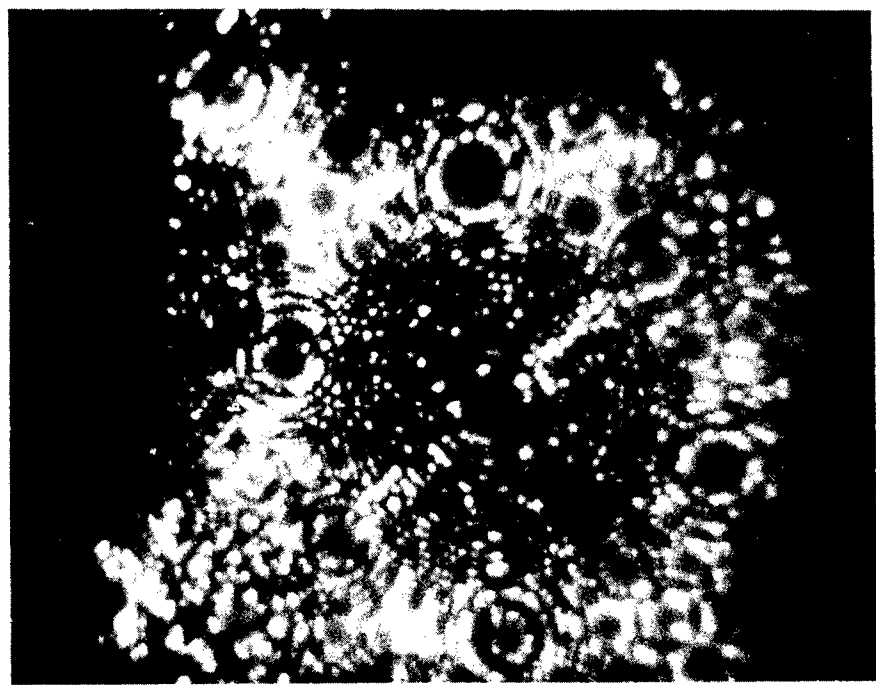


a

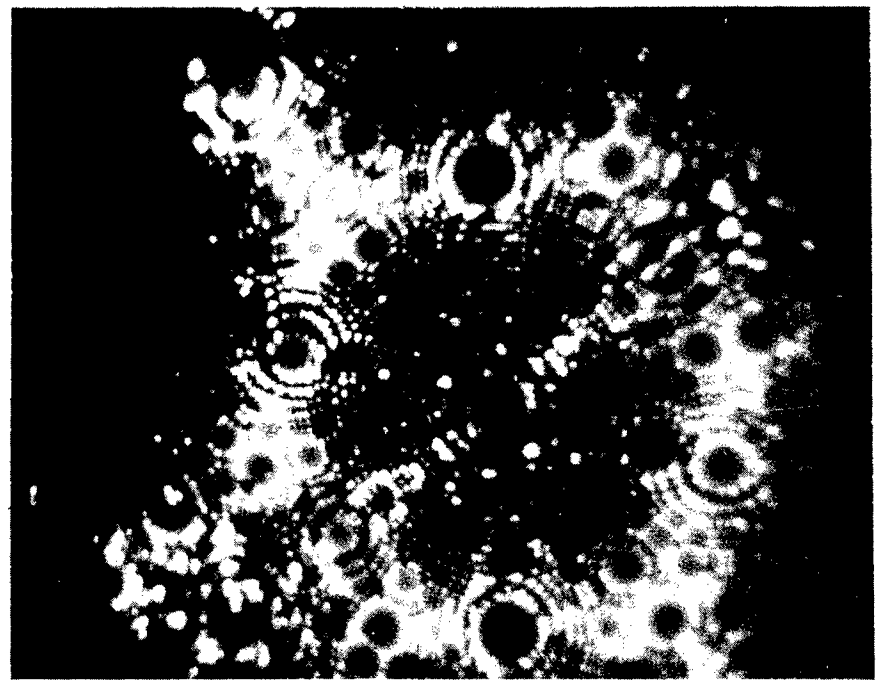


b

Figure 11. Tungsten in a $<110>$ orientation showing results of adsorption and desorption. a.) Clean tungsten surface imaged at $4.5 \text{ V}/\text{\AA}$ in 1.5μ of He. b.) Field reduced to $2.9 \text{ V}/\text{\AA}$ for 20 sec. to allow adsorption of residual vapors and reimaged at $4.5 \text{ V}/\text{\AA}$.



c



d

Figure 11. c.) Field raised to 5.4 V/Å for 30 sec. and reimaged at 4.5 V/Å . d.) Field raised to 5.4 V/Å for 60 additional sec. and reimaged at 4.5 V/Å . Surface has nearly recovered its former state.

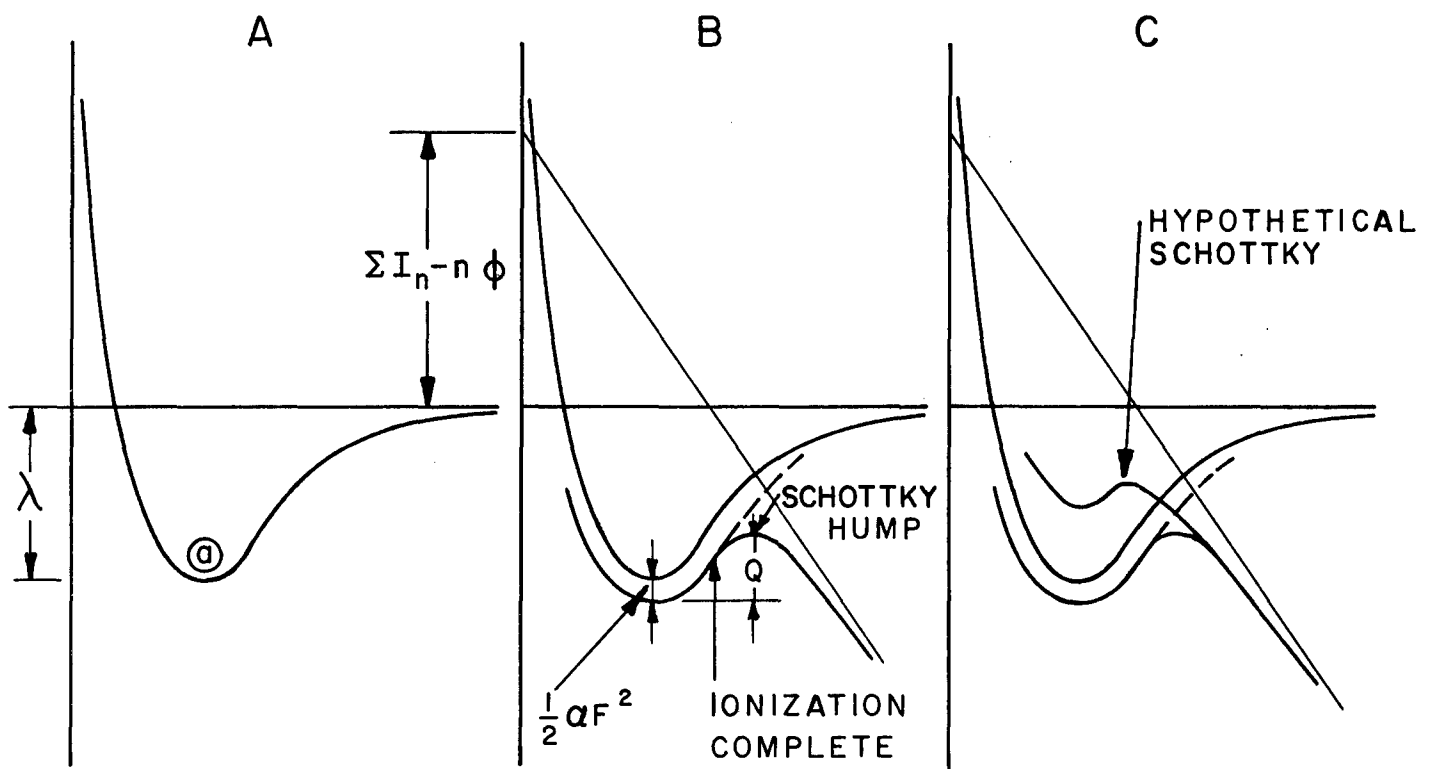


Figure 12. Potential energy curves applied to field evaporation.

a.) Without any field the atom rests in its potential well.

b.) Assuming complete ionization followed by evaporation of the ion over a Schottky hump. c.) Assuming Schottky hump to the left of the potential maximum. Adapted from Gomer and Swanson⁽¹⁷⁾.

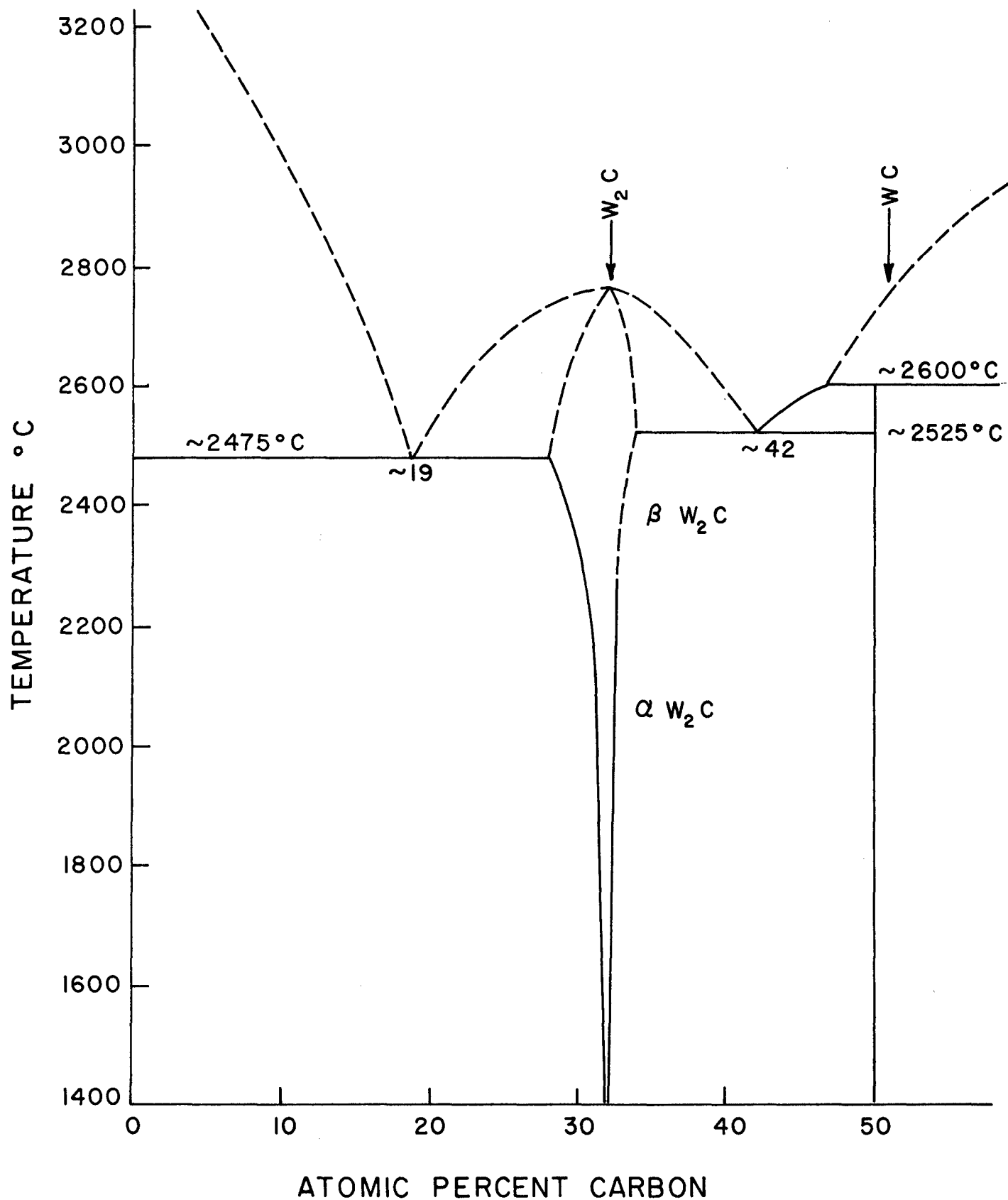


Figure 13. A partial tungsten-carbon phase diagram.

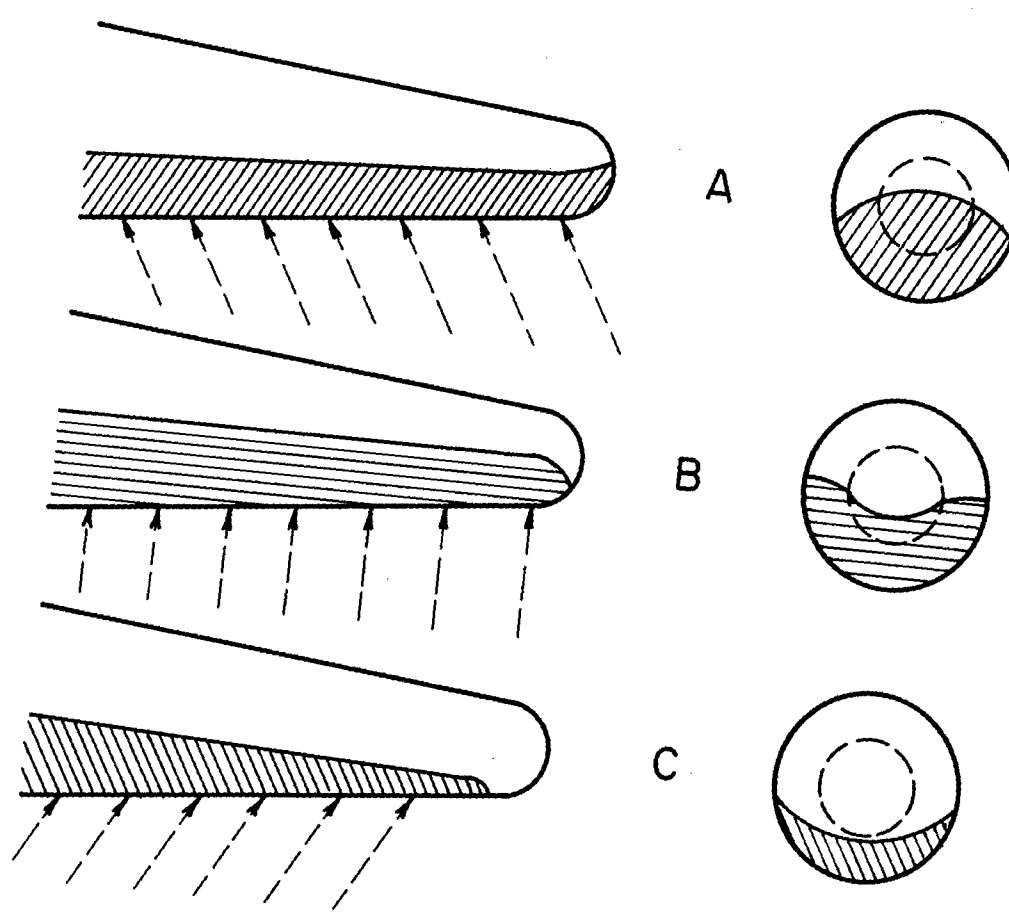
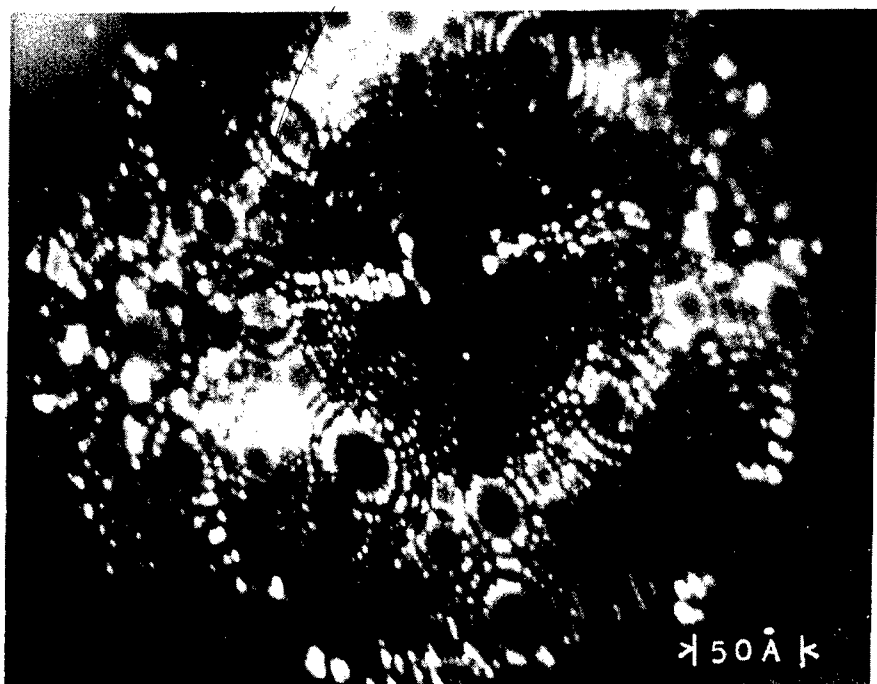
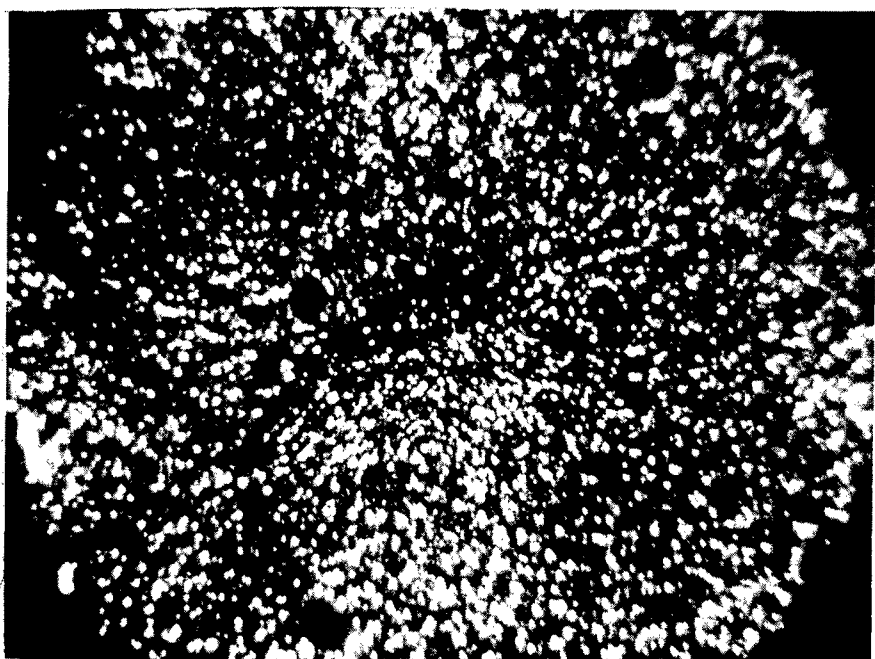


Figure 14. Dependence of deposit coverage on source location.
 a.) Source ahead of specimen. b.) Deposit impinging perpendicular to longitudinal axis of specimen. c.) Specimen ahead of source.
 After Gomer⁽⁴⁾.

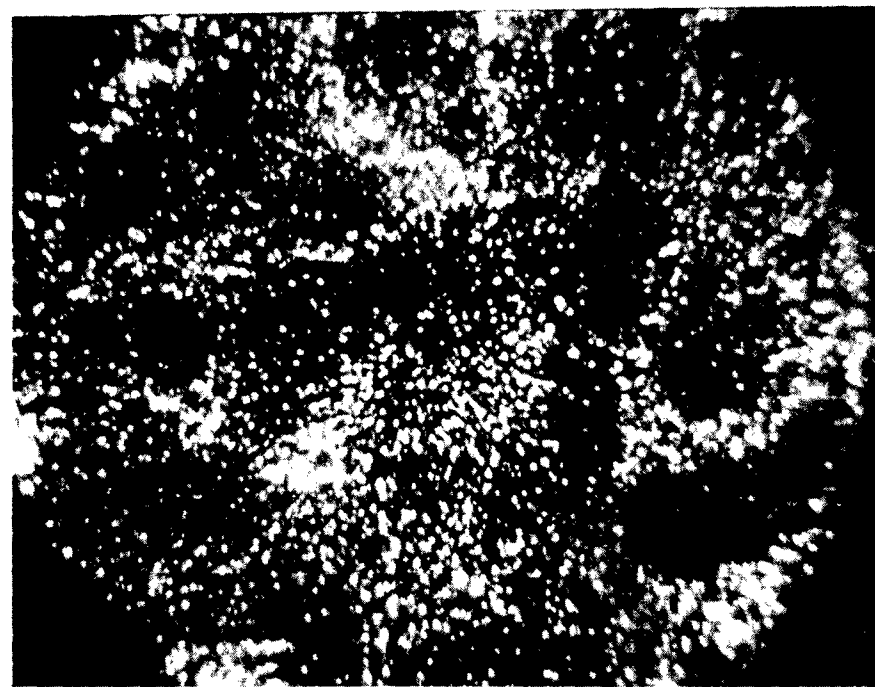


a

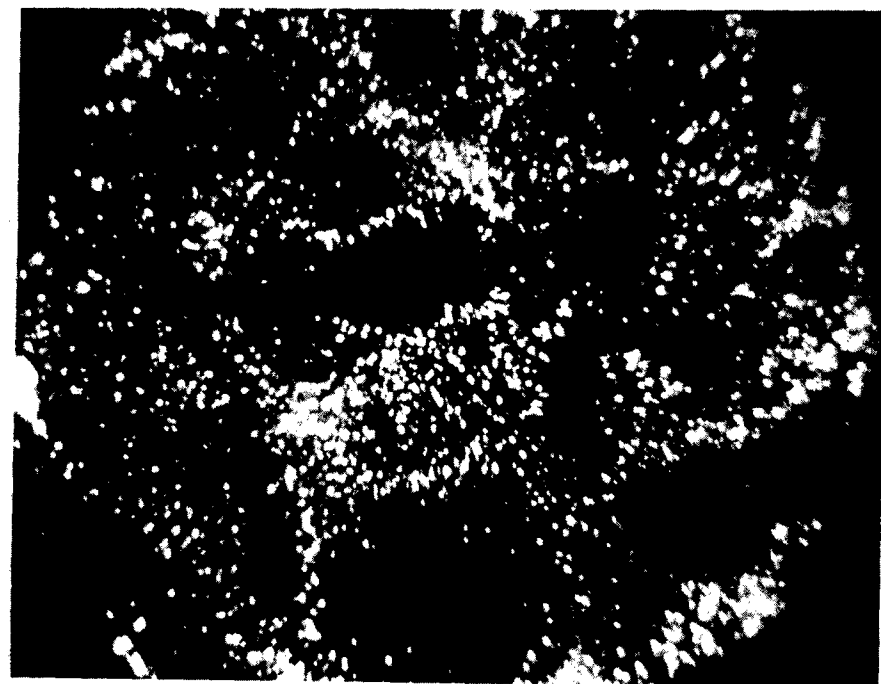


b

Figure 15. Tungsten-8 At.% Carbon. a.) Clean tungsten; 10,000V, 77°K. b.) Cold carbon deposit; 19,500V, 77°K.

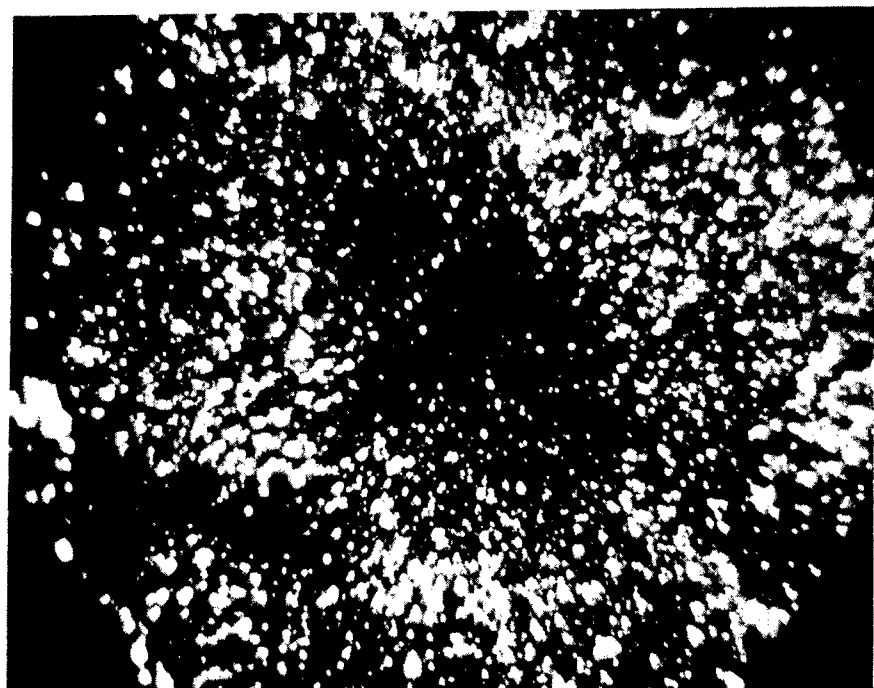


c

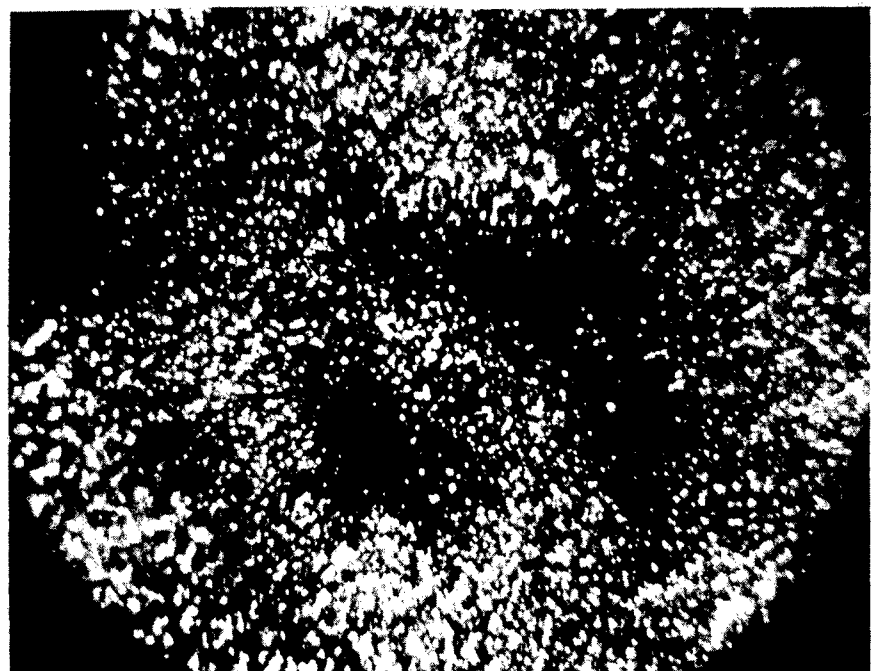


d

Figure 15. Tungsten-8 At.% Carbon (cont.) c.) Heated to $\sim 1500^{\circ}\text{C}$ for 2 sec; 19,400V. d.) Heated again to $\sim 1500^{\circ}\text{C}$ for 2 sec.; 19,400V.

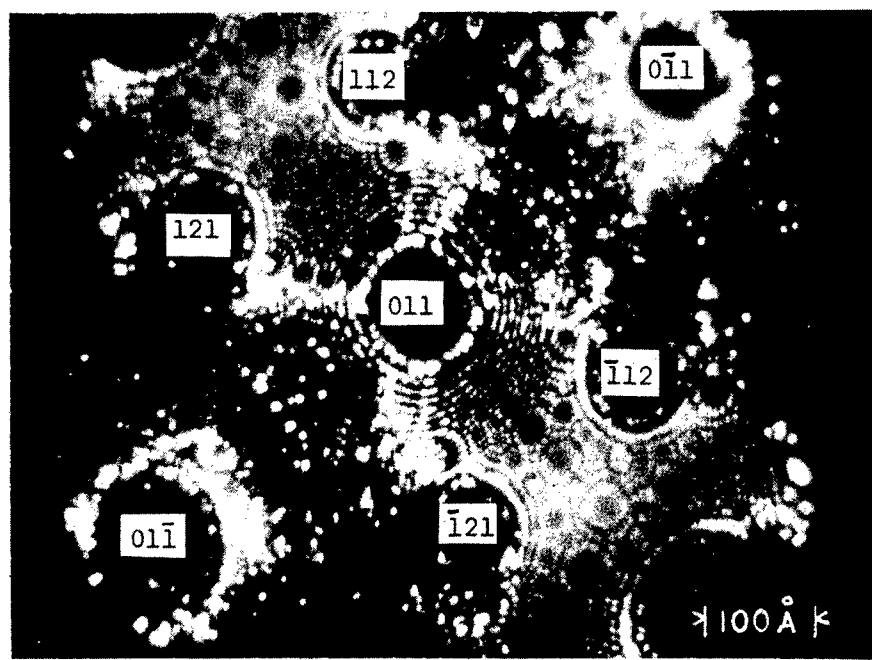


e

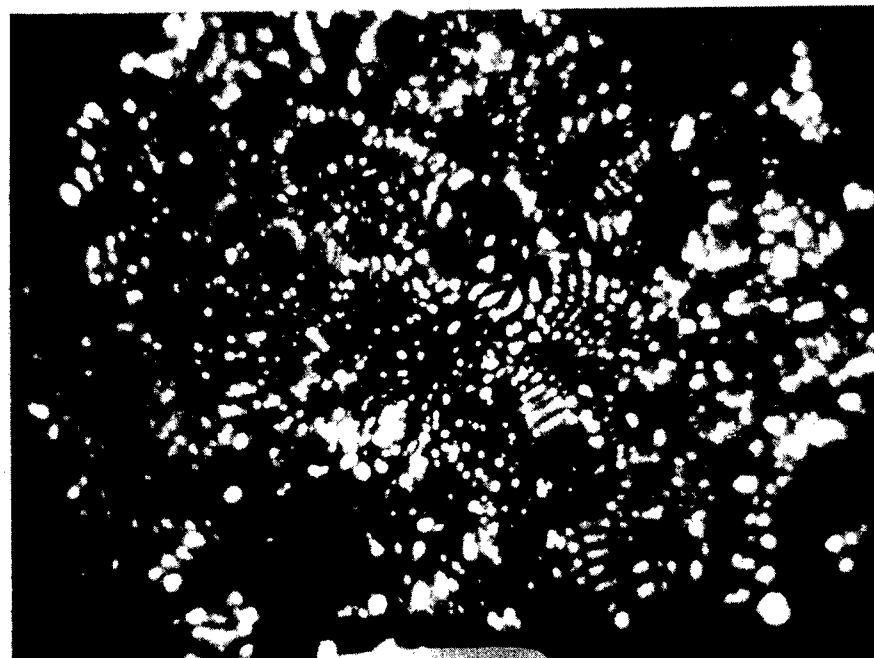


f

Figure 15. Tungsten-8 At.% Carbon (cont.) e.) Specimen breaking up under field applied stress; 19,400V. f.) Before specimen rupture; 22,500V.

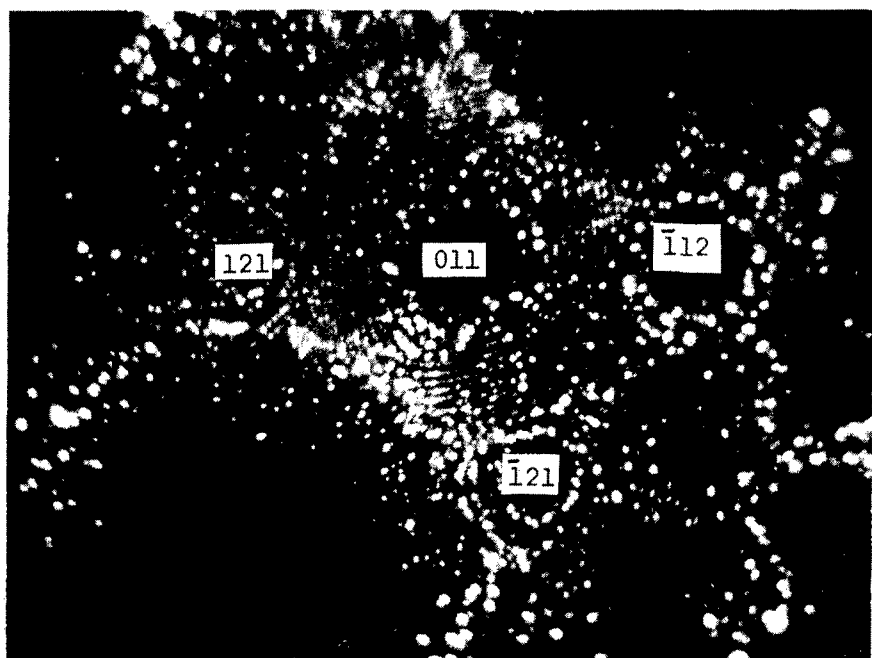


D

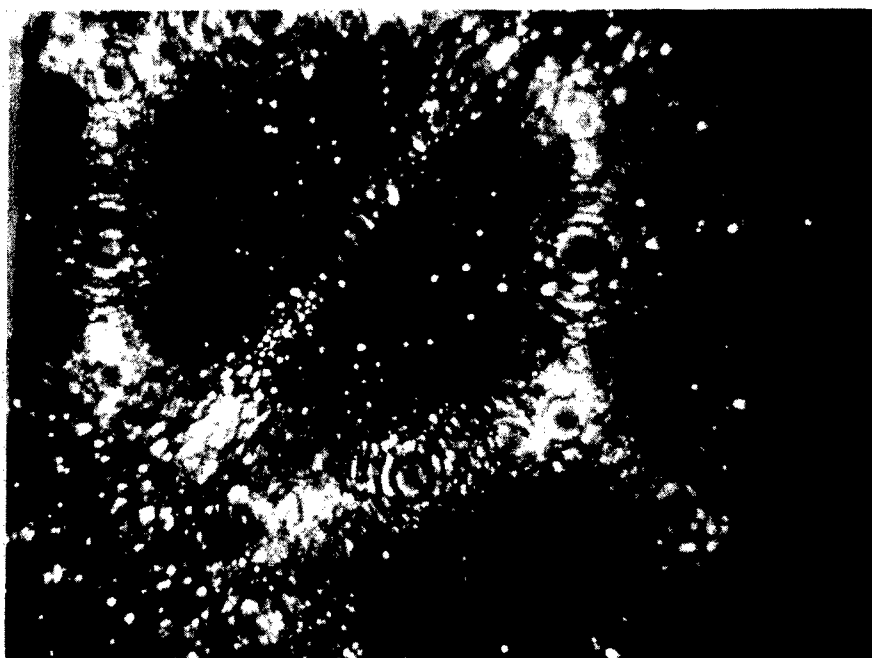


b

Figure 16. Tungsten-8 At.% Carbon. a.) Clean tungsten; 15,500V, 77°K, b.) Oriented overgrowth after carburizing; 13,600V, 77°K.

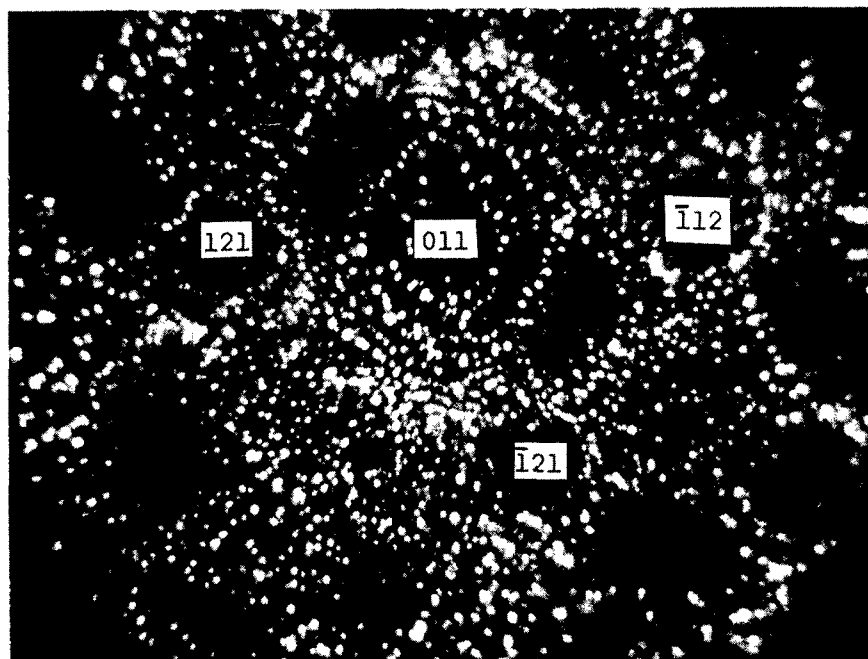


c

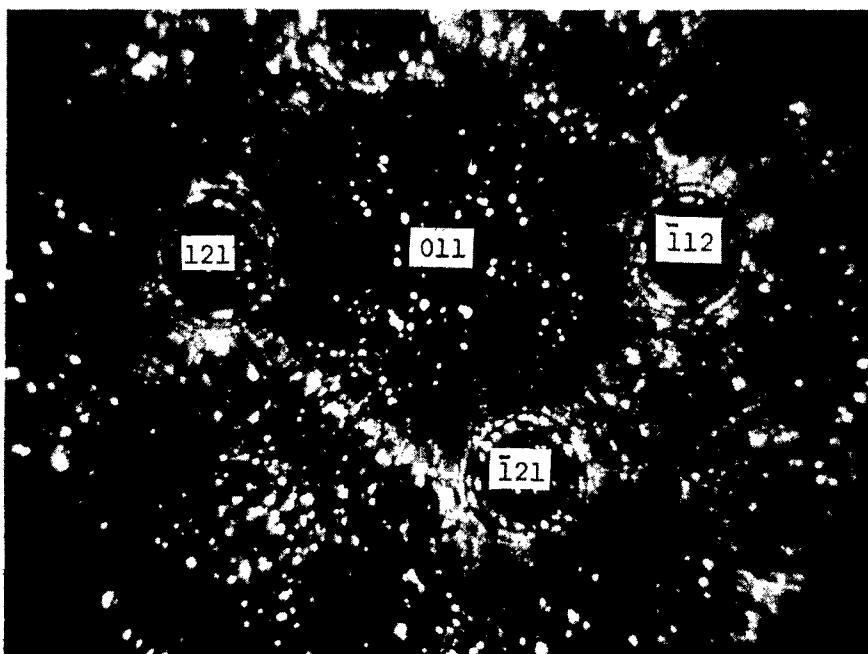


d

Figure 16. Tungsten-8 At.% Carbon (cont.) c.) After field evaporating the surface overgrowth layer; 14,900V. d.) Voltage pulsed to 20,000V, reimaged at 18,100V.

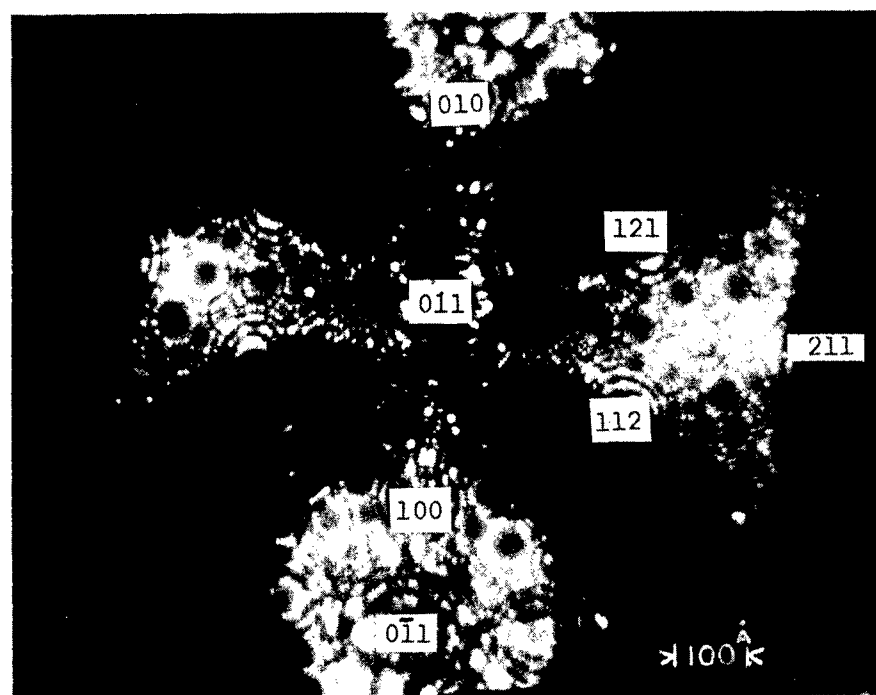


e

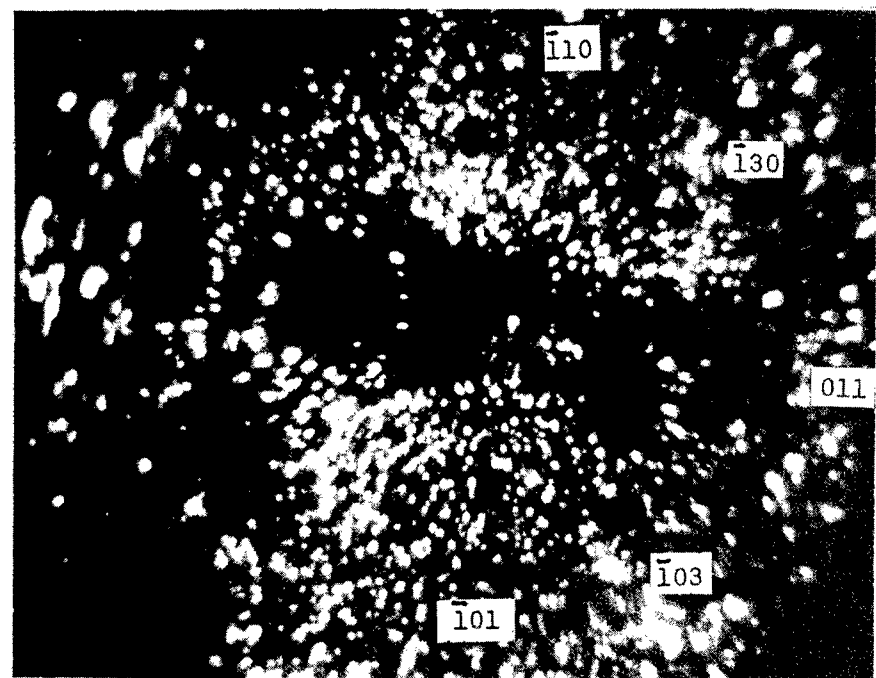


f

Figure 16. Tungsten-8 At.% Carbon (cont.) e.) Specimen heated to $\sim 1500^{\circ}\text{C}$ momentarily; 16,800V. f.) After removal of most surface impurities; 17,100V.

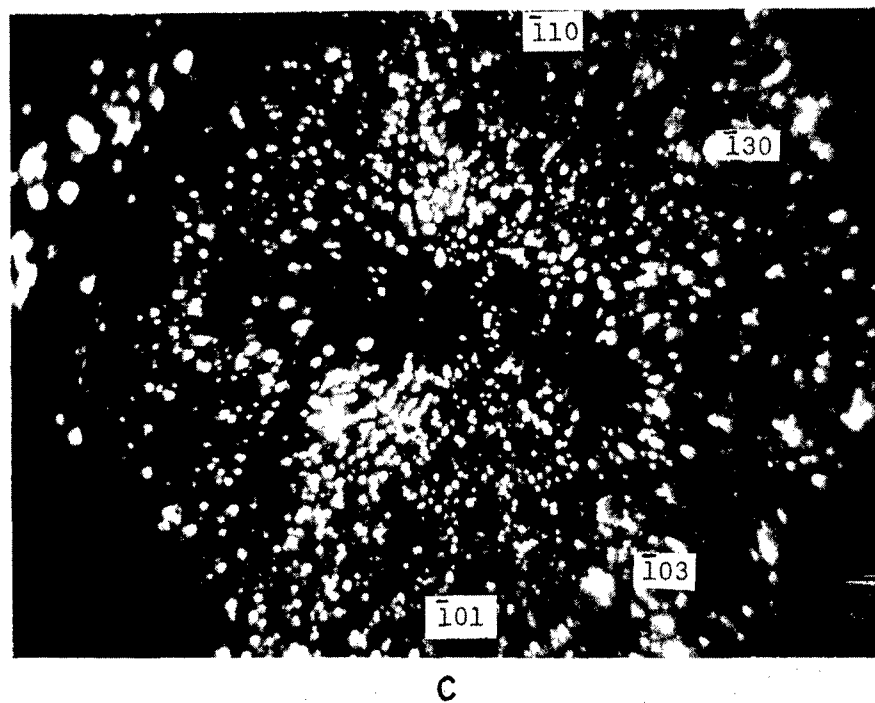


D

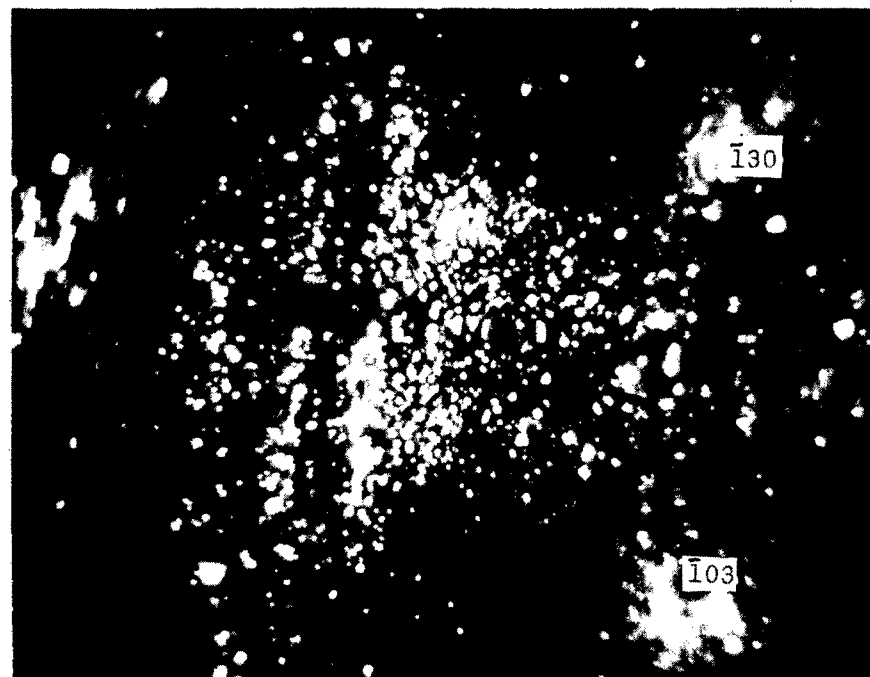


b

Figure 17. Tungsten-16 At.% Carbon. a.) Clean tungsten; 14,500V, 77°K. b.) After carburizing; 14,900V, 77°K.

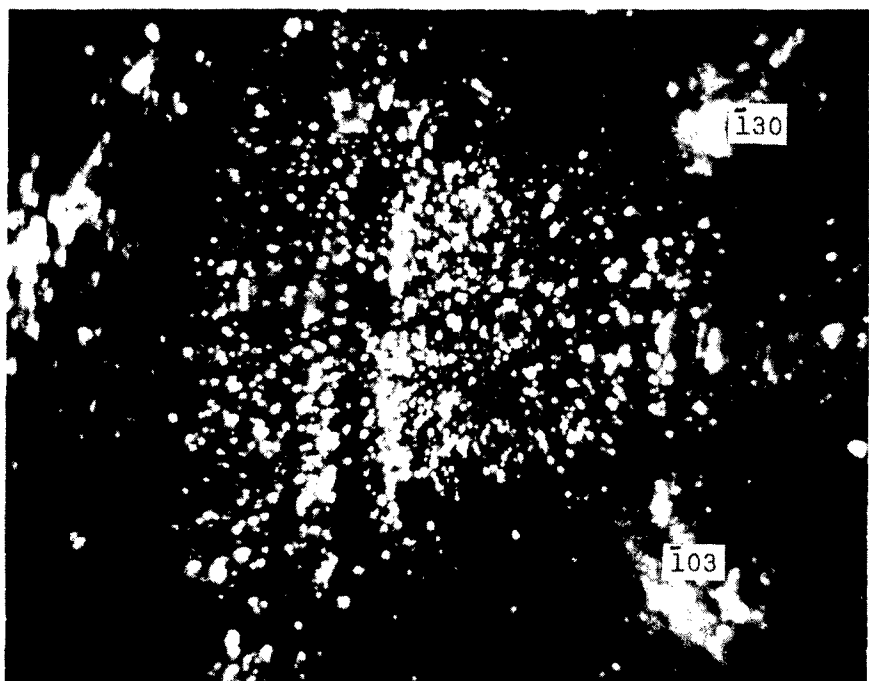


c

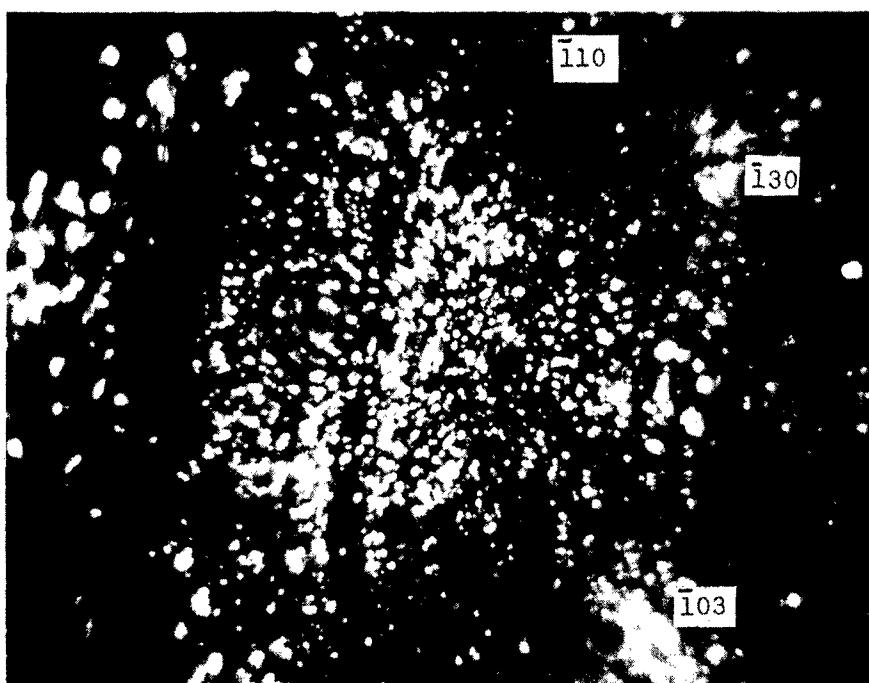


d

Figure 17. Tungsten-16 At.% Carbon (cont.) c.) Slip bands appear after voltage increase to 19,100V; 15,700V. d.), e.), f.) Successive stages of field evaporation; 15,700V, 16,700V, 16,900V.

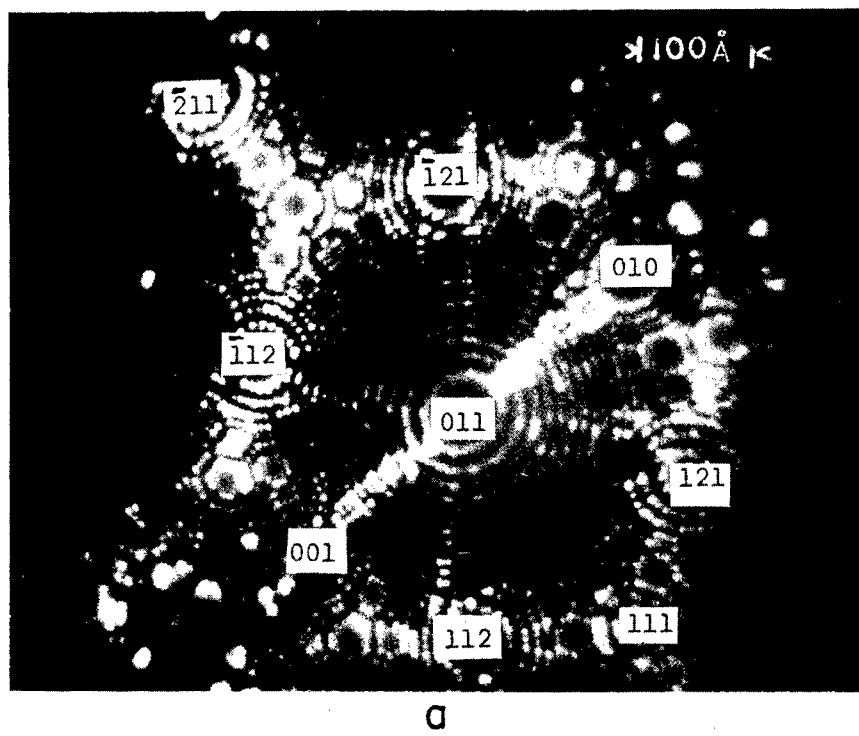


e

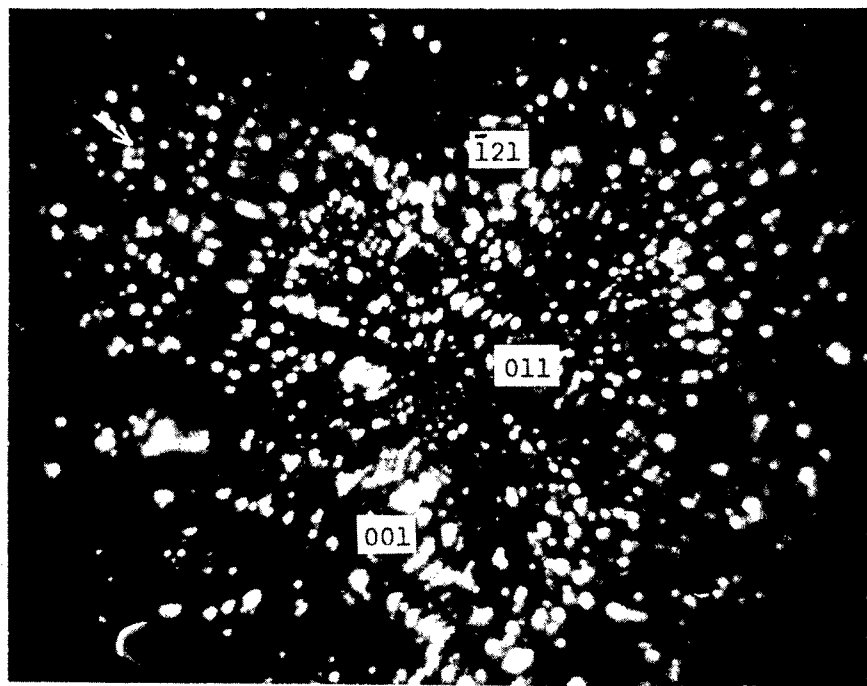


f

FIG. 17

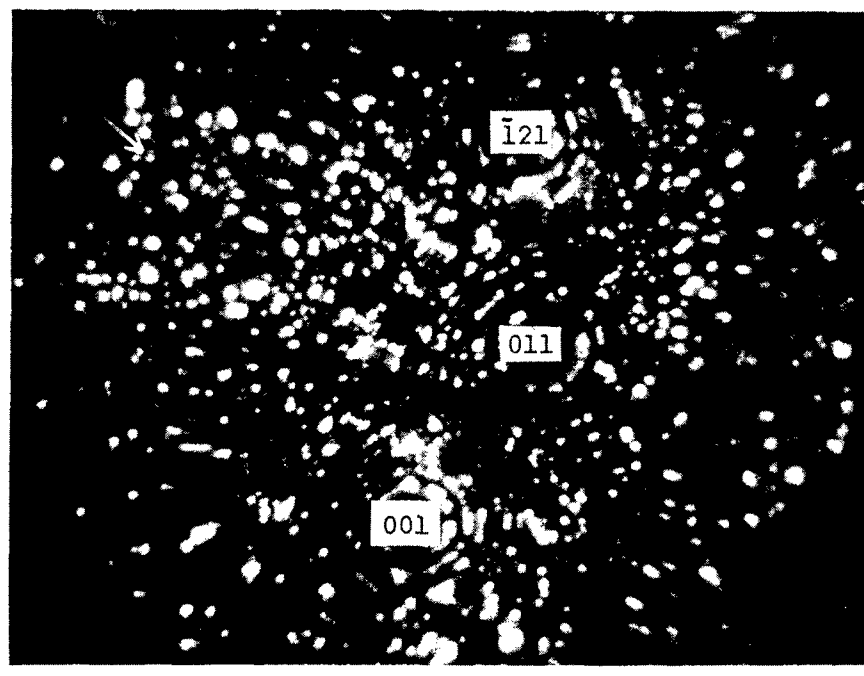


a

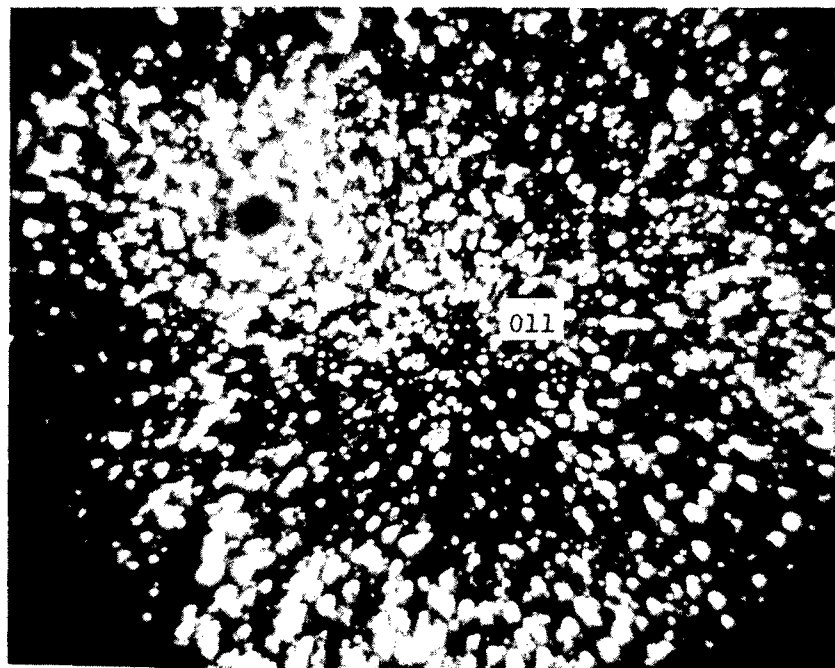


b

Figure 18. Tungsten-48 At.% Carbon. a.) Clean tungsten; 9250V, 77°K. b.) After diffusing in carbon in the direction indicated by the arrow; 9000V, 77°K.

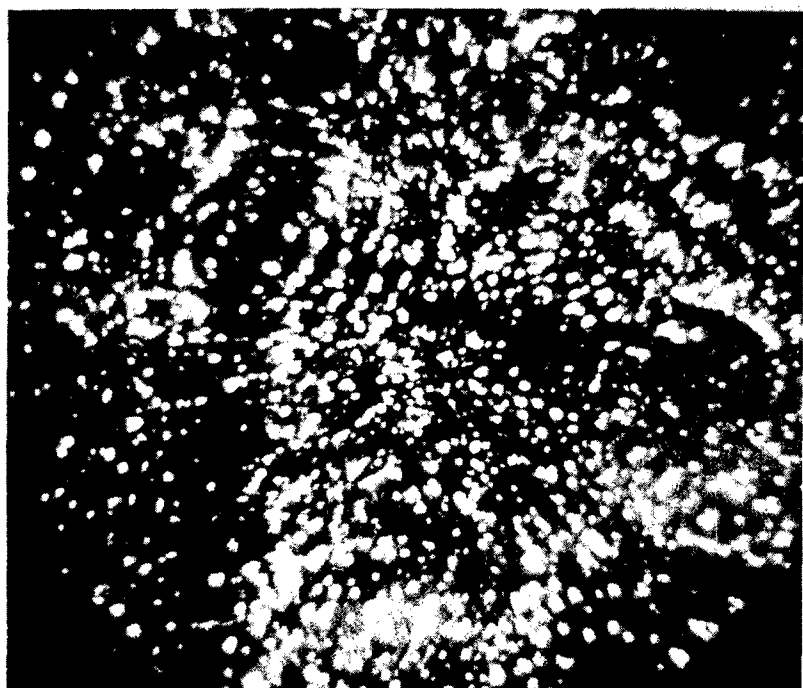


c

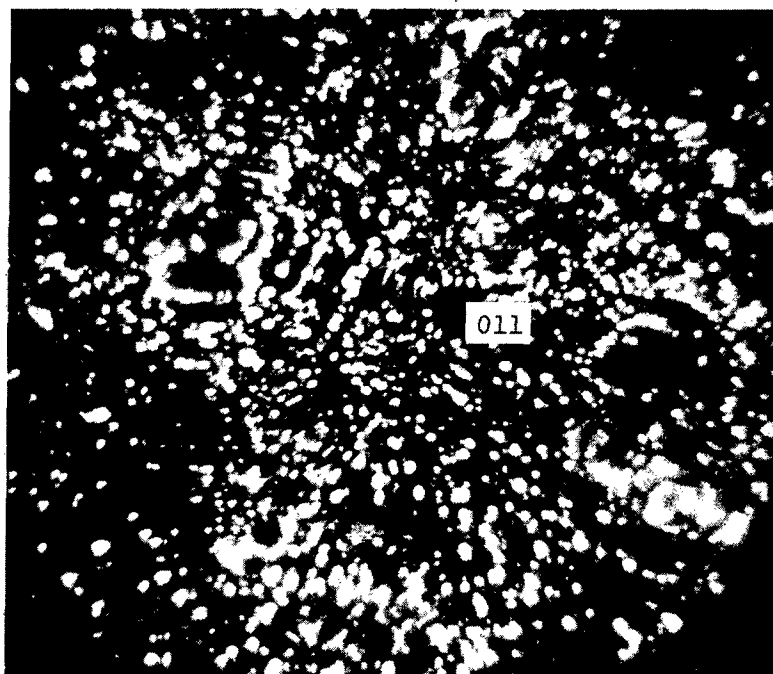


d

Figure 18. Tungsten-48 At.% Carbon (cont.) c.) After removal of one atom layer; 9100V. d.) Entire overgrowth layer removed; 13,300V.

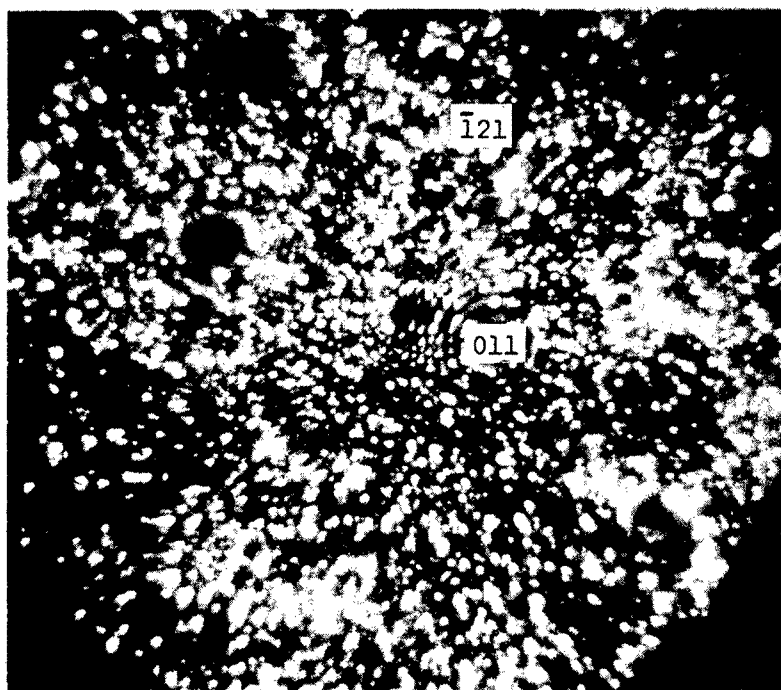


e



f

Figure 18. Tungsten-48 At.% Carbon (cont.) e.) After heating to ~ 1500°C for 10 sec. and field evaporating to clean the surface; 13,750V. f.), g.) Removal of several more planes indicates the original tungsten structure is returning; 14,250V.



g

FIG. 18